

Microscopic and Spectromicroscopic Insight and Fabrication of Nanoscaled Structures on Surfaces

Habilitation Thesis

to achieve the *venia legendi* in physical chemistry

submitted by

Dr. Hubertus Marbach

**Naturwissenschaftliche Fakultät II
Friedrich-Alexander-Universität Erlangen-Nürnberg**

Erlangen, February 2010

Contents

1	Introduction.....	7
2	STM investigations of porphyrins and phtalocyanines on single crystal metal surfaces [P1-P11].....	11
2.1	<i>Ordering aspects of porphyrins on Ag(111)and Cu(111)</i>	<i>12</i>
2.2	<i>In situ metalation of free base porphyrins and phthalocyanines</i>	<i>22</i>
2.3	<i>Spectromicroscopic investigations and electronic structure.....</i>	<i>26</i>
2.4	<i>Coadsorption of small molecules.....</i>	<i>30</i>
2.5	<i>Summary and current research activities.....</i>	<i>32</i>
3	Fabrication and characterization of nanostructures by means of a highly focused electron beam [P12-P16].....	35
3.1	<i>Results following the “classical” EBID protocol in UHV.....</i>	<i>39</i>
3.2	<i>Post treatment procedures</i>	<i>42</i>
3.3	<i>Catalytic effects</i>	<i>44</i>
3.4	<i>Summary, perspective applications and current project activities....</i>	<i>48</i>
4	Summary and Outlook.....	51
5	References	55
6	Acknowledgements	67
7	Appendix	69
7.1	<i>Personal data and scientific profile</i>	<i>69</i>
	Short Curriculum Vitae.....	69
	Funded projects (2004-2010):.....	70
	Cooperations and networks (2004-2010):.....	70
	List of publications:	72
	Invited presentations (2005-2010):	74
7.2	<i>Teaching (2004-2010) / in German.....</i>	<i>77</i>
8	Original publications	80

P1

83

F. Buchner; V. Schwald; K. Comanici; H. P. Steinrück; **H. Marbach***

Microscopic evidence of the metalation of a free-base porphyrin monolayer with iron

Chemphyschem **2007**, *8*, 241-243.

- P2** **89**
T. E. Shubina; **H. Marbach**; K. Flechtner; A. Kretschmann; N. Jux; F. Buchner;
H. P. Steinrück; T. Clark; J. M. Gottfried*
*Principle and mechanism of direct porphyrin metalation:
Joint experimental and theoretical investigation*
Journal of the American Chemical Society **2007**, *129*, 9476-9483.
- P3** **107**
F. Buchner; K. Comanici; N. Jux; H. P. Steinrück; **H. Marbach***
*Polymorphism of porphyrin molecules on Ag(111)
and how to weave a rigid monolayer*
Journal of Physical Chemistry C **2007**, *111*, 13531-13538.
- P4** **117**
K. Comanici; F. Buchner; K. Flechtner; T. Lukasczyk; J. M. Gottfried; H. P.
Steinrück; **H. Marbach***
*Understanding the contrast mechanism in scanning tunneling microscopy (STM)
images of an intermixed tetraphenylporphyrin layer on Ag(111)* Langmuir **2008**,
24, 1897-1901.
- P5** **125**
Y. Bai; F. Buchner; M. T. Wendahl; I. Kellner; A. Bayer; H. P. Steinrück; **H.
Marbach***; J. M. Gottfried*
*Direct metalation of a phthalocyanine monolayer on Ag(111) with coadsorbed
iron atoms*
Journal of Physical Chemistry C **2008**, *112*, 6087-6092.
- P6** **133**
F. Buchner; K. Flechtner; Y. Bai; E. Zillner; I. Kellner; H. P. Steinrück; **H.
Marbach***; J. M. Gottfried*
*Coordination of iron atoms by tetraphenylporphyrin monolayers and multilayers
on Ag(111) and formation of iron-tetraphenylporphyrin* Journal of Physical
Chemistry C **2008**, *112*, 15458-15465.

- P7** **143**
J. M. Gottfried* ; **H. Marbach**
Surface-Confined Coordination Chemistry with Porphyrins and Phthalocyanines: Aspects of Formation, Electronic Structure, and Reactivity
Zeitschrift Fur Physikalische Chemie **2009**, *223*, 53-74.
- P8** **167**
F. Buchner; I. Kellner; H. P. Steinrück; **H. Marbach***
Modification of the Growth of Iron on Ag(111) by Predeposited Organic Monolayers
Zeitschrift Fur Physikalische Chemie **2009**, *223*, 131-144.
- P9** **183**
Y. Bai; F. Buchner; I. Kellner; M. Schmid; F. Vollnhals; H. P. Steinrück; **H. Marbach***; J. M. Gottfried*
Adsorption of cobalt (II) octaethylporphyrin and 2H-octaethylporphyrin on Ag(111): new insight into the surface coordinative bond
New Journal of Physics **2009**, *11*.
- P10** **201**
F. Buchner; K. G. Warnick; T. Wölfle; A. Görling; H. P. Steinrück; W. Hieringer* ; **H. Marbach***
Chemical Fingerprints of Large Organic Molecules in Scanning Tunneling Microscopy: Imaging Adsorbate-Substrate Coupling of Metalloporphyrins
Journal of Physical Chemistry C **2009**, *113*, 16450-16457.
- P11** **229**
F. Buchner; K. Seufert; W. Auwärter; D. Heim; J. V. Barth; K. Flechtner; J. M. Gottfried; H. P. Steinrück; **H. Marbach***
NO-Induced Reorganization of Porphyrin Arrays
Acs Nano **2009**, *3*, 1789-1794.
- P12** **237**
O. Guise; **H. Marbach**; J. Levy; J. Ahner; J. T. Yates*
Electron-beam-induced deposition of carbon films on Si(100) using chemisorbed ethylene as a precursor molecule
Surface Science **2004**, *571*, 128-138.

- P13** **251**
T. Lukasczyk; M. Schirmer; H. P. Steinrück; **H. Marbach***
*Electron-beam-induced deposition in ultrahigh vacuum:
Lithographic fabrication of clean iron nanostructures*
Small **2008**, *4*, 841-846.
- P14** **259**
T. Lukasczyk; M. Schirmer; H. P. Steinrück; **H. Marbach***
*Generation of Clean Iron Structures by Electron-Beam-Induced Deposition and
Selective Catalytic Decomposition of Iron Pentacarbonyl on Rh(110)*
Langmuir **2009**, *25*, 11930-11939.
- P15** **271**
M.-M. Walz; M. Schirmer; F. Vollnhals; T. Lukasczyk; H. P. Steinrück;
H. Marbach*
Electrons as Invisible Ink - Generation of Iron Nanostructures on 300 nm SiO_x
2010, *submitted*.
- P16** **291**
M. Schirmer; M.-M. Walz; F. Vollnhals; T. Lukasczyk; C. Chen; H. P. Steinrück;
H. Marbach*
*Addressing Proximity Effects in Electron Beam Induced Deposition:
Fabrication of Clean Titanium Oxide Nanostructures on Silicon*
2010, *to be submitted*.

Acronyms

2HOEP	octaethylporphyrin
2HPc	phthalocyanine
2HTPP	5,10,15,20-tetraphenylporphyrin
2HTTBPP	5,10,15,20-tetrakis-(3,5-di-tert-butyl)-phenylporphyrin
AES	Auger electron spectroscopy
AFM	atomic force microscope
DBP	di-tert-butyl-phenyl
DFG	Deutsche Forschungsgemeinschaft
DOS	density of states
EBID	electron beam induced deposition
ECCL	electron controlled chemical lithography
EM	electron microscope
FEBIP	focused electron beam induced processing
HOMO	highest occupied molecular orbital
HV	high vacuum
LDOS	local density of states
LEED	low energy electron diffraction
LT	low temperature
LUMO	lowest unoccupied molecular orbital
MOEP	metallo-octaethylporphyrin (M = Co, Ni...)
MPc	metallo-phthalocyanine (M = Fe, Co..)
MTPP	metallo-tetraphenylporphyrin (M = Fe, Co, Zn...)
MTTBPP	metallo-5,10,15,20-tetrakis-(3,5-di-tert-butyl)-phenylporphyrin (M = Fe, Co...)
PtMe₃Cp'	Trimethyl-methylcyclopentadienyl-platinum
QMS	quadrupole mass spectrometry
RT	room temperature
SAM	scanning Auger microscopy
SEM	scanning electron microscopy
SFB	Sonderforschungsbereich
SPM	scanning probe microscopy
STM	scanning tunneling microscope
STS	scanning tunneling spectroscopy
TEM	transmission electron microscope
TTIP	titanium tetraisopropoxide
UHV	ultra high vacuum
UV	ultraviolet
VT	variable temperature
XPS	x-ray photoelectron spectroscopy

1 Introduction

The concept of the atom as the undividable smallest building block of matter was already introduced around 400 B.C. by the ancient Greek philosophers Demokrit and Leukipp. At this time the actual observation or even manipulation of atoms was certainly pure fiction. It took another 2000 years till optical microscopy advanced such that insights into nature on scales beyond human perception became possible (e.g., van Leeuwenhoek [1]). In classical microscopy the ultimate resolution limit is determined by the wavelength of the light used to image an object, i.e., for light in the visible range the ultimate limit is roughly 400 nm. One idea to push the ultimate resolution is to employ radiation with shorter wavelength. With this approach Ernst Ruska successfully explored electrons as illumination source resulting in the development of the first operable electron microscope (EM) surpassing the performance of conventional light microscopes in 1933. A different route to improve the resolving power is the concept of sensing the object based on near-field interactions (scanning probe microscopy, SPM). The first and most prominent example of such a microscope is the scanning tunneling microscope (STM), which was invented in 1982 by Gerd Binnig and Heinrich Rohrer [2]. STM enabled mankind to actually “see” single atoms in real space on flat surfaces more than 2000 years after their proposal by Demokrit*. The importance of both, the electron microscope and the STM, can be illustrated by the award of the Nobel price in physics to Ruska, Binnig and Rohrer in 1986. Nowadays different types of EMs and SPMs are established and widely spread as state-of-the-art microscopes in science and industry. Without the possibility to image with nanometer or even atomic resolution on a daily basis the emergence of nanotechnology would have not been possible. Generally, advancing miniaturization means an increasing density of functional entities. For semiconductor industry this trend, i.e., the increasing number of transistors per area with time, is quantitatively described in Moore’s law [4]. Considering the newest generation industrial production of integrated circuits the smallest features are already fabricated with 32 nm half pitch. The ultimate limit for miniaturization is the atomic dimension itself; interpolating Moore’s law this restriction will be reached within the next decades. It is easy to understand that electrical conductivity, e.g., in a string of copper atoms, is different to the one in a macroscopic lead made from the same material. But already objects in the nanometer regime exhibit all sorts of size effects like quantum confinement or enhanced catalytic activity. In short, miniaturization below a certain size implies new effects and thus novel potential applications, which

* The first microscope to deliver atomic resolution (restricted to sharp metallic tips) was the field ion microscope developed by Erwin W. Müller.[3.]

are the main reason for the boost of nanotechnology in the last decades and which are closely related to the development of high resolution microscopes. In this context the field of surface science certainly has played a key role as one of the major driving forces. Here, the huge arsenal of available spectroscopic, microscopic, spectromicroscopic tools and preparation methods in combination with the well defined experimental conditions (ultra high vacuum (UHV), single crystal samples) enabled valuable insight into basic physical and chemical properties of nanoscaled structures.

Besides the characterization, the controlled fabrication of functional nanostructures is in the focus of current research and development. Therein one can distinguish two main routes:

- In the **bottom-up** approach complex structures are assembled in a controlled manner from small building blocks, in particular from atoms or/and molecules. The arrangement can be realized through molecular recognition in a self-assembly process or by directed positioning of the single entities (e.g., positioning of atoms with an STM).

- The **top-down** approach includes patterning techniques traditionally applied in semiconductor industry like UV- or electron beam-lithography. Hereby externally controlled larger components (e.g. an electron beam) are used to fabricate structures from smaller entities (e.g. molecules).

In the framework of this Habilitation thesis both concepts were successfully applied in two main projects with a common surface science approach, i.e., the structures were fabricated on single crystal surfaces in UHV, mostly at room temperature (RT) with well defined, pure materials.

The subject of the first project is the STM investigation of large organic molecules [5-8], namely porphyrins [9-15], on metal surfaces (Ag(111), Cu(111)) [P1-P11]. These molecules are considered ideal building blocks for the engineering of functional molecular architectures since they combine an intrinsic functionality with a rigid molecular frame, which often triggers long range order [P7]. The functionality of the molecules is thereby mainly determined by the coordinated metal atom. Prominent examples for porphyrins as main functional building blocks in nature are iron porphyrins in heme [16-18] and magnesium porphyrins in chlorophyll [19]. A central aspect of the experiments in this Habilitation thesis was to gain insight into the processes causing long range ordered structuring of the porphyrins as a prototype example for a bottom-up approach. In this regard different supramolecular

arrangements could be observed, depending on the peripheral substituents of the porphyrins, the substrate, (in some cases) the coordinated metal atom and coadsorbed small molecules. The corresponding results allow to gain deeper understanding of the contributions of molecule-molecule and molecule-substrate interactions in the particular systems and thus to propose strategies to tailor porphyrin architectures. Another aspect was the exploration of a novel route to synthesize metalloporphyrins, namely the *in situ* metalation and thus functionalization of free base porphyrins in the experimental chamber under UHV conditions. The metalation of porphyrins upon evaporation of different metals was studied in great detail and the underlying mechanisms could be elucidated [P1, P2, P5-P7]. Since STM data always reflect both the topography and the local density of states (LDOS) of the investigated object it was crucial to achieve insight into the electronic interaction of the porphyrin and the substrate. Spectromicroscopic data was acquired via bias dependent STM and scanning tunneling spectroscopic (STS) methods. In combination with complementary information from theory (Andreas Görling, Wolfgang Hieringer, Erlangen) and spatially averaging photoelectron spectroscopy (Michael Gottfried, Erlangen) fundamental aspects of the adsorbate-substrate electronic interaction could be revealed. For example, the bias dependent appearance of a cobalt porphyrin could be traced back to a specific hybrid orbital of the adsorbate complex [P10]. In the framework of the Sonderforschungsbereich 583 “Redox-Active Metal Complexes: Control of Reactivity via Molecular Architecture”, located in Erlangen, the following collaborations contributed to establish the comprehensive and detailed picture of the porphyrin-metal systems: Michael Gottfried (photoelectron spectroscopy), Wolfgang Hieringer, Andreas Görling, Tatyana Shubina, Timothy Clark (theory), Norbert Jux and Nicolai Burzlaff (synthesis). Low temperature STM data from Wilhelm Auwärter and Johannes Barth (TU Munich) also added valuable information to the investigation of porphyrin films with coadsorbed nitrogen oxide.

In the second part of this thesis the generation and characterization of arbitrarily shaped, clean nanostructures is targeted by means of focused electron beam induced processing (FEBIP), i.e., in a top-down approach [P12-P16]. Our starting point was to use a highly focused electron beam (diameter < 3 nm) of an UHV compatible scanning electron microscope (SEM) to locally crack adsorbed precursor molecules, resulting in a deposit of the nonvolatile dissociation products (electron beam induced deposition, EBID [20-23]). In the corresponding experimental setup a hemispherical electron analyzer also enabled to acquire spectroscopic and spectromicroscopic information of the deposited structures based on local Auger spectroscopy. Recently FEBIP became technologically relevant, as it superseded focused ion beam based

methods as the state-of-the-art mask repair tool in semiconductor industry [24], due to the comparably smaller achievable sizes of generated structures [25, 26]. Among numerous advantages of EBID is the wide spread of SEMs as standard microscopic tools in science and industry and the availability of a huge arsenal of suitable precursor molecules. The vision is that by the choice of the right precursor, e.g., an organometallic compound, the fabrication of a corresponding pure metallic deposit can be realized. Generally the vast majority of EBID experiments are performed in high vacuum (HV) environments resulting in deposits with rather poor metal contents of typically 10 to 60 at. % from organometallic precursors [20, 27-39]. One idea of working under ultra clean conditions, i.e., UHV, was to reduce contaminations stemming from the unintended deposition of residual gases. Another aspect was to perform EBID in surface science type experiments to ensure well defined, reproducible conditions. Indeed in our surface science approach to EBID we were not only able to generate metallic nanostructures with an unprecedented purity [P13-P16], but also discovered several effects not observed in HV based investigations before. The experiments performed in the work at hand are focused on two molecules, namely ironpentacarbonyl ($\text{Fe}(\text{CO})_5$) as precursor for iron deposits [P13-P15] and titanium tetrakisopropoxide (TTIP) as precursor for titaniumoxide deposits [P16]. In both cases very clean deposits could be achieved [P13-P16]. One example is the generation of extremely small ($\sim 4 - 8$ nm diameter) iron nanodots from $\text{Fe}(\text{CO})_5$ on Si(001) in a surface mediated process [P13] Other important findings were the occurrence of catalytic and autocatalytic effects already at room temperature [P14, P15] and directly linked to that the importance of clean conditions, which can only be realized in UHV. Another main finding is the possibility to locally activate different silicon oxide surfaces by electron irradiation as seed for the growth of Fe nanostructures from $\text{Fe}(\text{CO})_5$ [P15]. This example expands FEBIP significantly and might be the brink of a whole new route to write nanostructures.

With the results mentioned above and additional findings presented in this thesis a considerable expansion of the FEBIP tool box is established. Besides the novel perspectives for the fabrication of nanostructures we also explored general methodic and instrumental aspects. These concern, e.g., limitations of the SEM hardware, the lithographic attachment, the interaction of electrons with the sample as well as general issues of SEM and local AES investigations in surface science.

The work at hand is organized as a cumulative thesis, i.e., a short review of main findings of the attached papers is presented together with important unpublished results, which are partially discussed in greater detail.

2 STM investigations of porphyrins and phtalocyanines on single crystal metal surfaces [P1-P11]

The STM investigation of large organic molecules on surfaces has become a vivid field in science with the vista to engineer functional devices [5-8]. The confinement on the surface in combination with molecular recognition either between absorbed molecules and/or specific substrate sites often triggers the self-assembly of long range ordered arrays. In this regard porphyrins or more generally tetrapyrrools appear to be ideal building blocks for the generation of functional molecular devices, since they combine their rigid planar framework as a structure forming element with an intrinsic functionality, mainly determined by the coordinated metal center. The targeted applications for porphyrin based architectures comprise catalysis [40-43], sensors [44-48] and solar energy conversion [49-51]. Prototype examples can be found in nature, where in particular metallotetrapyrrools play a decisive role in important biological processes. The most prominent examples are: iron porphyrins in heme [16-18], magnesium porphyrins in chlorophyll [19] and cobalt corrin in vitamin B₁₂. These examples, which are also depicted in Figure 2.1. illustrate that the functionalities of the porphyrins are apparently determined by the corresponding central metal atom but also a contribution from the different substituents and environments must be considered. Therefore the investigation of porphyrins on surfaces under well defined conditions might also deliver valuable insights into the much more complex processes in nature.

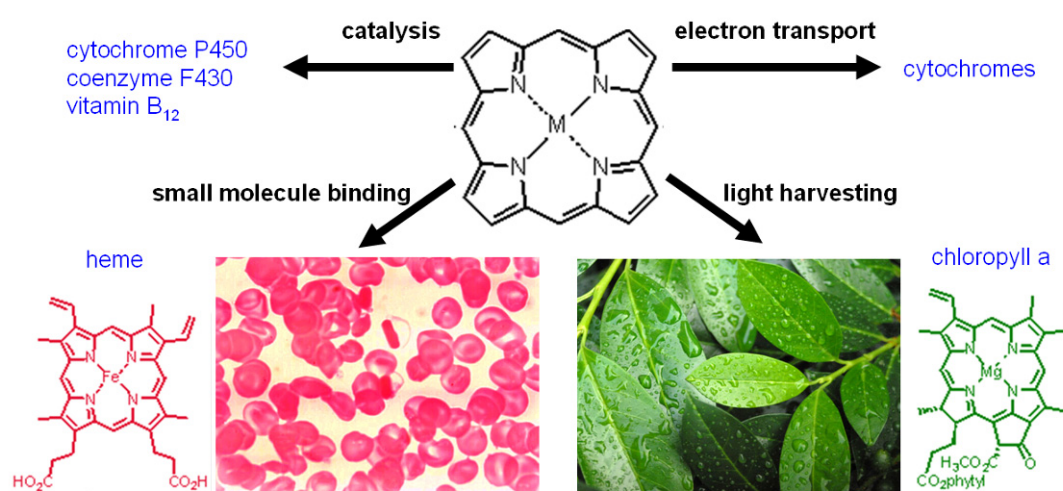


Figure 2.1 Illustration of the different functionalities of metalloporphyrins in nature.

In this work well defined (111)-oriented surfaces of copper and silver were used as substrates for different tetrapyrrolic molecules. All experiments and the preparation of the surface as well as the thermal evaporation of the molecules onto the surfaces were conducted under ultra clean, i.e., UHV conditions. The instrument used was a RHK UHV VT STM 300 with RHK SPM electronics. The experimental setup was subsequently improved during the course of this project: to start with, the mechanical and electronic setup was fine tuned such that atomic resolution became possible, the cooling setup was optimized for both liquid and precooled gaseous nitrogen, a mass spectrometer up to amu 2000 (Pfeiffer, HiQuad QMG700) was purchased and installed, the tunneling current sensitivity was increased by one order of magnitude with a corresponding preamplifier (Femto, DLPCA-200) and the electronics were upgraded. The vast majority of the experiments were conducted at RT in distinction to numerous low temperature measurements published so far (e.g. [10, 52-54]). This is an important detail, since these conditions are simply more realistic for both the production of molecular architectures and as model systems for processes in nature.

The main topics of the investigations were: aspects concerning the ordering behavior of the porphyrins (self assembly of supramolecular arrays, intramolecular conformation), in situ metalation of porphyrins, electronic structure (LDOS) of the adsorbate complex and the interaction of ordered porphyrin layers with small molecules. Correspondingly the results are discussed in four subchapters even though the classification of the observations is partially not sharp.

2.1 Ordering aspects of porphyrins on Ag(111)and Cu(111)

The engineering of functional devices based on the self-assembly of large organic molecules, e.g., porphyrins requires a detailed knowledge of the underlying processes in order to control the formation of the molecular building blocks on the surface. Thus it is vital to gain a deeper understanding of the relevant processes, i.e., to identify the driving forces, which determine the self-assembly of the molecular components. In this context the specific contributions of molecule/substrate and molecule/molecule interactions are in the focus of the investigations to be discussed below. In Figure 2.2. STM images of a well prepared Ag(111) surface are depicted. The most important feature is the identification of the six fold symmetry given by the three main directions of the closed packed atomic rows as indicated by the green arrows in Figure 2.2 b, which is also the case for the Cu(111) surface (not shown here).

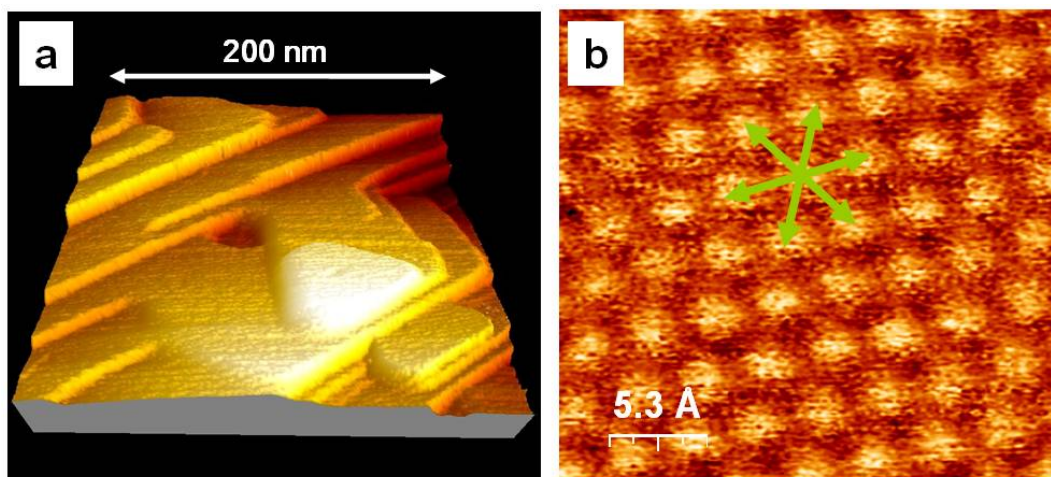


Figure 2.2 Constant current RT STM images of a well prepared Ag(111) surface. **a)** Large scale STM data in a 3D-plot exhibiting single and multiple atomic steps. A typical feature is the triangularly shaped island. Acquisition parameters were: $I_{set} = 1 \text{ nA}$, $U_{gap} = -430 \text{ mV}$. **b)** STM image with atomic resolution exhibiting a hexagonal closed packed arrangement of the silver atoms characteristic for the (111) plane of fcc crystals. The noisy character of the image stems most probably from diffusing silver atoms (due to high mobility of silver at RT). Acquisition parameters were: $I_{set} = 0.85 \text{ nA}$, $U_{gap} = -40 \text{ mV}$.

The porphyrin derivatives investigated in the framework of the current Habilitation project are depicted in Figure 2.3. One idea was to tune the metal center-substrate distance and thus interaction by attaching different “bulky” peripheral substituents as indicated in the lower row of Figure 2.3 [56]. Equally important, the variation of the side groups might also alter the intermolecular interactions [9, 12-15, 57-60]. In distinction to the threefold symmetry of the fcc (111) surfaces the individual porphyrins apparently exhibit a fourfold symmetry (or twofold for 2HOEP) in the “naive” conformation depicted in Figure 2.3. Each porphyrin derivative can exist with a metal center or as free base porphyrin with two terminal hydrogen atoms coordinated to two nitrogen atoms, as represented by the 2HOEP. Consequently, two chemically nonequivalent nitrogen pairs (iminic, pyrrolic) can be distinguished by means of x-ray photoelectron spectroscopy (XPS) [61, 62] [P2, P5-P7, P 11]. STM results on Ag(111) will be discussed starting with the molecules in the left column of Figure 2.3, i.e., with octaethylporphyrins. The details of the corresponding investigation can be found in [P9].

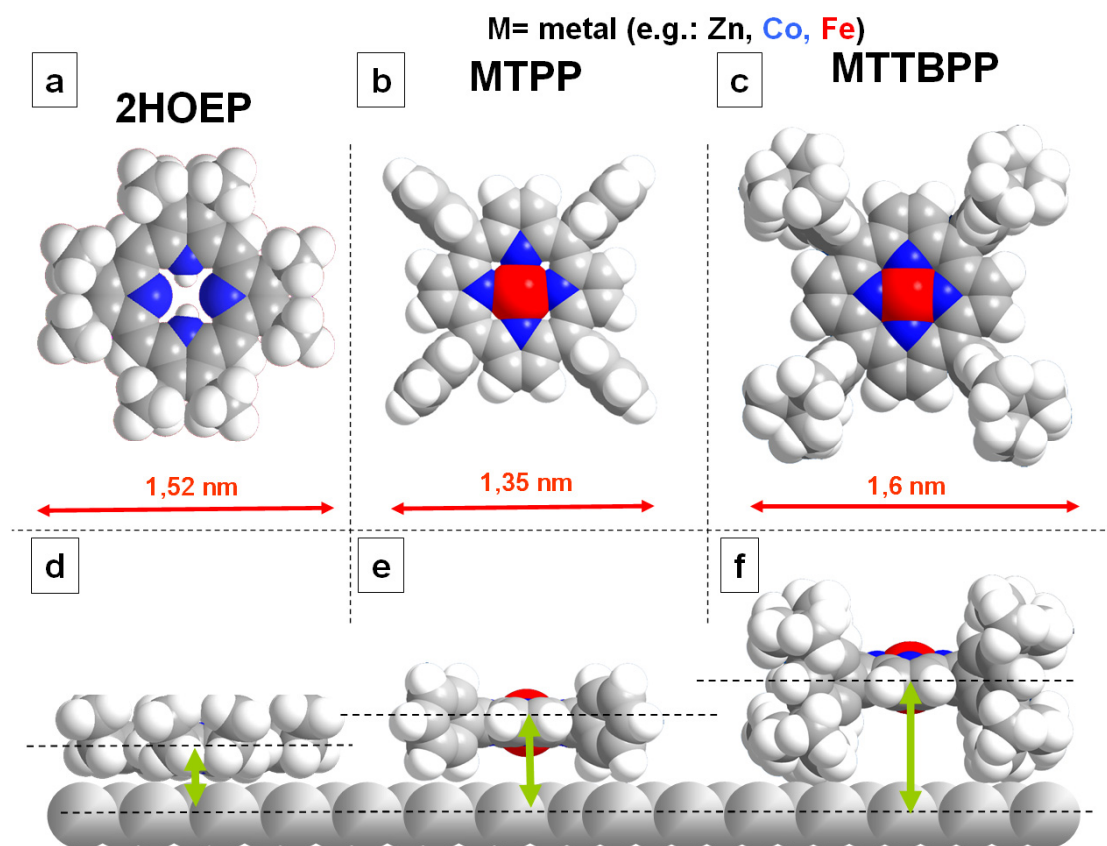


Figure 2.3 Space-filling models of: **a), d)** 2H-2,3,7,8,12,13,17,18-octaethylporphyrin (2HOEP); **b), e)** metallo-5,10,15,20-tetraphenylporphyrin (MTPP) and **c), f)** metallo-5,10,15,20-tetrakis-(3,5-di-tert-butyl)-phenylporphyrin (MTTBPP). The depicted models are drawn with a “naive” intramolecular conformation, i.e. without further geometry optimization.

For that purpose a mixture of 2HOEP and CoOEP was thermally evaporated onto the substrate. At RT meaningful STM micrographs could only be acquired if the Ag(111) surface was completely covered with porphyrins. This could be comprehensively interpreted as due to high mobility of the molecules at the given conditions (RT). It is therefore evident that neither the molecule/substrate nor the intermolecular interactions are strong enough to fix single OEPs or ensembles of OEPs below monolayer coverage. Typical results for an ordered 2HOEP/CoOEP monolayer are shown in Figure 2.4. The main ordering theme resembles an almost hexagonally closed packed arrangement. This type of array is in line with the dense confinement of high symmetry objects in a plane, e.g., if one pushes coins or pin pong balls together on a table top they will exhibit this order.

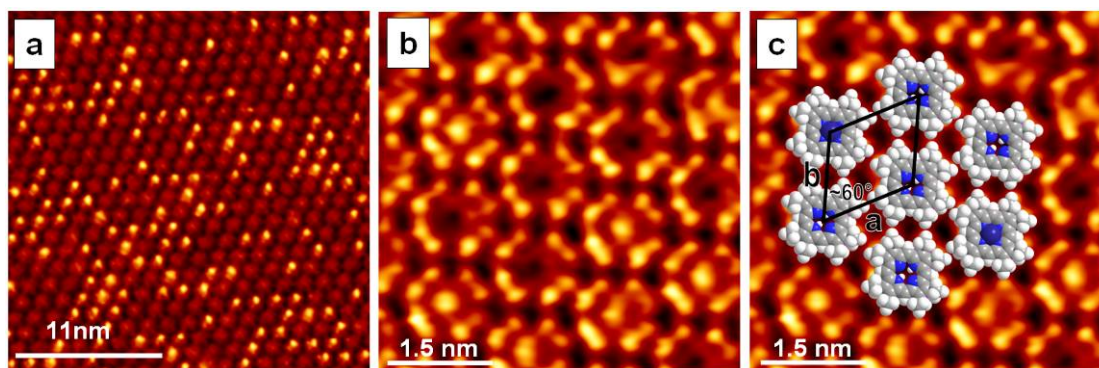


Figure 2.4 STM micrograph of an intermixed 2HOEP/CoOEP layer prepared by vapor-deposition of a nominal 2:1 mixture of the respective species onto the Ag(111) surface. Counting over large areas results in 34% protrusions, which can be identified with CoOEP molecules. Tunneling parameters: $I_{set} = 31$ pA, $U_{gap} = -1.17$ V. **a), b)** STM micrograph of a self-assembled intermixed 2HOEP/CoOEP layer on Ag(111). Tunneling parameters: $I_{set} = 37$ pA, $U_{gap} = -0.20$ V. In **c)** the micrograph is superimposed by scaled models of the corresponding OEP molecules and the unit cell is indicated ($a = 1.55 \pm 0.10$ nm, $b = 1.45 \pm 0.10$ nm). The figure is adapted from [P9]

A similar mechanism can be assumed for the observed ordered structure, even though a certain influence of the surface on the orientation of the domains can not be ruled out. In Figure 2.4 a, a single molecule is represented by one protrusion. The bimodal appearance can be conclusively explained by identifying the brighter spots with CoOEP and the dimmer with 2HOEP. The high resolution STM data depicted in Figure 2.4 b evidences the adsorption geometry with the undistorted porphyrin plane parallel to the Ag(111) surface. The submolecular resolution in combination with overlaid scaled models in Figure 2.4 c enable to identify the intramolecular features like the four ethyl pairs and the central cobalt atom for CoOEP as well as the central cavity for 2HOEP. The increased apparent height of the side groups in comparison with the porphyrin ring indicates that the ethyl groups are indeed pointing away from the substrate, as sketched in Figure 2.3 a and d and in line with previous investigations of similar systems [60, 63-67].

The most intensively studied molecular species in the current project were tetraphenylporphyrins [P1, P2, P4, P6-P8, P10, P11]. In Figure 2.5 the Ag(111) surface is imaged at medium resolution for different coverage of CoTPP (a, b) and ZnTPP (c); with individual metalloporphyrins always appearing as a single protrusions. At very low coverage the CoTPP molecules can exclusively be observed as chains of single bright dots at the lower side of the step edges with an intermolecular distance of roughly 1.4 nm (Figure 2.5 a).

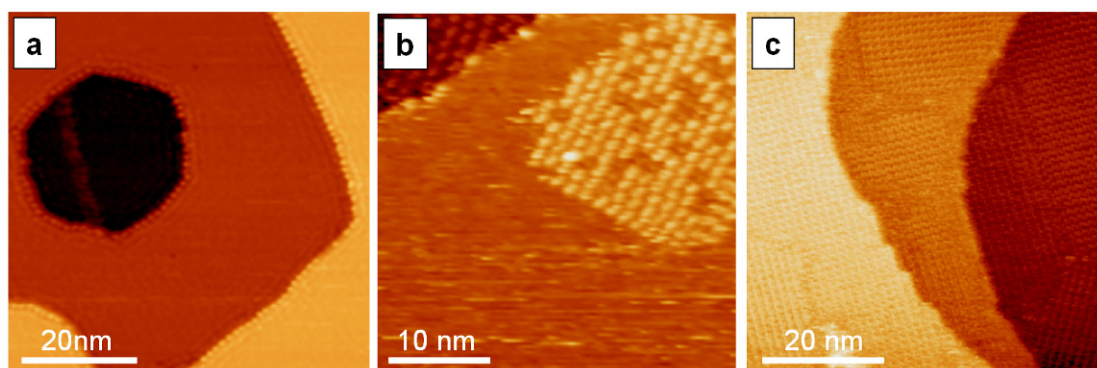


Figure 2.5 STM images of TPPs on Ag(111) acquired at different coverages θ_{abs} . (a) The Ag(111) steps are decorated with CoTPP at a low coverage ($U = -1.25$ V, $I = 15$ pA). (b) Two-dimensional CoTPP islands evolve at medium coverage ($U = -1.20$ V, $I = 255$ pA). (c) Monolayer of ZnTPP ($U = -1.22$ V, $I = 500$ pA).

Since basically all observed molecules are located at the steps, their diffusion length at room temperature (RT) must exceed the width of the corresponding terraces [68, 69] [P8]. Obviously the step edge constitutes an energetically favorable adsorption site for the porphyrin. It can be concluded that in the very low coverage regime the molecule/substrate interaction at these specific sites dominates the arrangement of the molecules. At a CoTPP coverage of roughly $\Theta_{abs} = 0.3$ ML the formation of ordered islands is observed (Figure 2.5 b, please note that $\Theta_{abs} = 1$ ML refers to the amount TPP needed to completely cover the surface). Within these islands the molecules arrange in a square order with a lattice constant of ~ 1.4 nm. Since the four fold symmetry of the molecular assemblies agrees with the intrinsic symmetry of a single molecule but deviates from the six fold substrate symmetry one has to conclude that molecule/molecule interactions account for the self assembly by mutual stabilization. Another important hint is the observation of the latter arrangements (square, ~ 1.4 nm lattice constant) for TPPs on different substrates [11, 13-15, 57] [P1, P2, P4, P6-P8, P10, P11], which indicates that the self assembly is indeed largely independent of the substrate. The noisy, stripy features in the bottom of Figure 2.5 can be assigned to molecules diffusing on the surface. The formation of the islands can then be understood as a condensation process, if one treats the molecules as a 2D gas [70]. Figure 2.5 c depicts ordered domains of a monolayer ZnTPP on Ag terraces. Again the molecules assemble in a square fashion with a lattice constant of 1.4 ± 0.05 nm. Since the identical ordering behavior was also found for 2HTPP [P1, P2, P6], FeTPP [P1, P6, P8] and CoTPP [P2, P7] it appears to be a general property of TPP on Ag(111).

More information can be obtained from high resolution micrographs: Figure 2.6 a reveals the particular submolecular and supramolecular features of CoTPP adsorbed

on Ag(111). First of all individual CoTPP molecules appear as elongated protrusions at the given tunneling conditions, i.e., when imaging the HOMO states. The origin of the specific appearance lies in the conformational adaptation upon adsorption as illustrated in Figure 2.6 b. The phenyl rings experience a considerable rotation compared to the “naive” conformation (with an angle of 90° relative to the porphyrin macrocycle) depicted in 2.3 b. As a result of the repulsion between the orthosubstituents the porphyrin ring is distorted such that two opposing pyrrole groups are bent towards and two away (marked yellow in Figure 2.6 b) from the surface [13, 57, 71] [P6-P9]. The observed appearance in STM is correspondingly dominated by the saddle-shape topography, i.e. the upper pyrrole groups and the central metal atom. Based on this information the detailed arrangement of the molecules can be determined as shown in Figure 2.6 c. The supramolecular order is such that each phenyl ring is pointing towards the center of a neighboring phenyl ring [72-74]. This results in an attractive T-type interaction of the corresponding π -systems [75, 76] known e.g. from liquid and crystalline benzene [77, 78]. This is an illustrative example how a rather simple microscopic information reveals the chemical nature of a supramolecular interaction and in the specific case the driving force for the self-assembly of TPP molecules on Ag(111). Another peculiar property of such ordered molecular assemblies on surfaces is the inherent organizational chirality [75, 79-82].

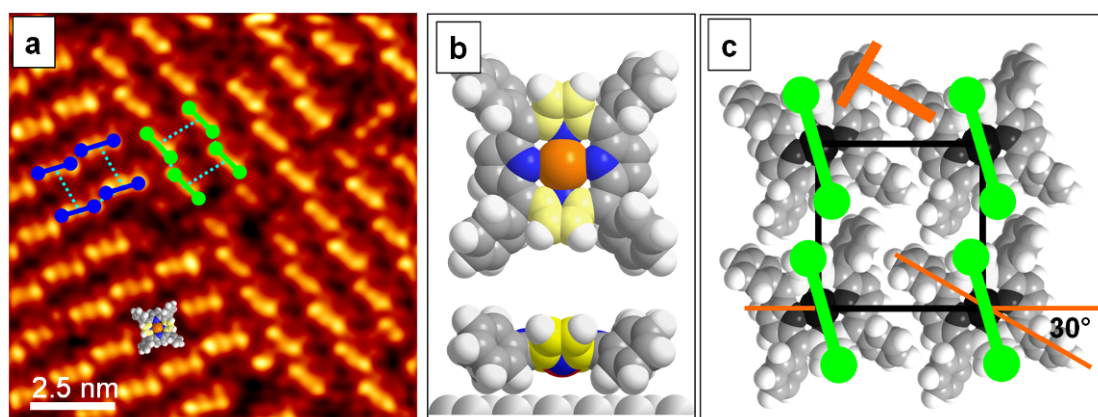


Figure 2.6 *a)* High resolution STM image of a CoTPP array with a domain border on Ag(111) ($U = -1.18$ V, $I = 56$ pA). *b)* Proposed intramolecular conformation of CoTPP on Ag(111). The two bent up pyrrole rings (marked yellow) determine the appearance of individual molecules in a). *c)* Extracted assembly of tetraphenylporphyrins. The driving force for the intermolecular attractive interactions is identified as a T-type interaction of the phenyl rings (indicated by an orange T). The arrangement exhibit organizational chirality as indicated by the dumbbells in c) and a). Observed domain boundaries always separate two domains of different chirality.

The square arrangement indicated by the green dumbbells in the experimental data (Figure 2.6 a) and the model (Figure 2.6 c) can only be transferred into the molecular order indicated by the blue dumbbells in 2.6 a by a mirror operation but not by translation and rotation in the plane. Thus the two arrangements exhibit different chirality in the plane. Remarkably, it was found in the work at hand that regardless of the actual TPP species all observed domain boundaries are at the same time separation lines between the enantiomers. It can thus be assumed that the specific organizational chirality limits the long range order of the domains. In summary, for the ordering of tetraphenylporphyrins on Ag(111) the T-type interaction in between the phenyl rings of neighboring molecules is identified as the driving force for the observed self-assembly in square order.

Changing the substrate from Ag(111) to Cu(111) the properties of adsorbed 2HTPP change drastically in terms of arrangement, appearance in STM and diffusion at RT [72, 83]. The individual 2HTPP molecules in Figure 2.7a appear as two elongated parallel protrusions. This shape can be understood by the topography of the proposed adsorption geometry sketched in Figure 2.7 c. Here the most elevated parts of the free base porphyrin are colored yellow [83]. The difference compared to the shape of, e.g., CoTPP on Ag(111) can be explained firstly by the central depression and secondly by the reduced stress in the macrocycle, both due to the lack of a metal center. The 2HTPPs exhibit only three azimuthal orientations, whereby the protrusions are aligned along the three closed packed high symmetry directions of the Cu substrate, presumably independent of the actual coverage. Obviously for free base tetraphenyl porphyrin on Cu(111) molecule/substrate interactions dominate the molecular arrangement. Furthermore, the diffusion is also restricted to the high symmetry directions, i.e., it is confined to one dimension as can be concluded from Figure 2.7 b and f. The reduced mobility of 2HTPP on Cu(111) enables to track the movement of the individual molecules and to extract the corresponding hopping rates. Based on the determination of such hopping rates at different temperatures it was possible to evaluate the activation barrier for surface diffusion in an Arrhenius plot according to [84, 85]. The migration barrier for 2HTPP on Cu(111) is $E_m = 0.69 \pm 0.09$ eV; this value is very similar to the one recently estimated by Eichberger et al. for the similar 2H-tetraperydylporphyrin on the same substrate [84]. The proposal of the specific interaction of 2HTPP with the Cu substrate is based on the observation that CoTPP self-assemble in the similar way on Cu(111) and on Ag(111), i.e., in a square order starting with island formation at a certain coverage (compare Figure 2.5). The differences in the adsorption behavior of ,e.g., CoTPP and 2HTPP on Cu(111) are revealed in Figure 2.7 e.

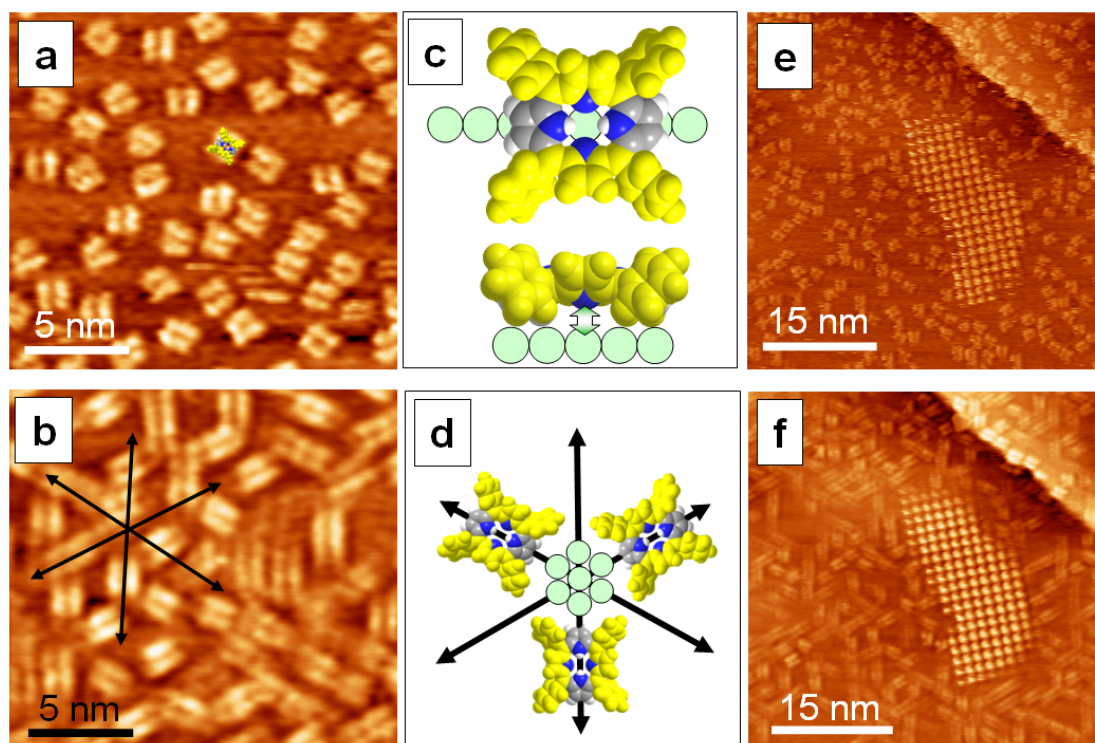


Figure 2.7 *a)* High resolution RT STM micrograph of 2HTPP molecules on Cu(111) ($U = -0.77$ V, $I = 26$ pA). *b)* Average image of subsequently acquired STM data (15 frames, ~ 50 min total) demonstrating the directional diffusion of 2HTPP along the closed packed atom rows of Cu(111). *c), d)* Sketches illustrating the proposed attractive interaction of the pyrrolic nitrogen atoms of 2HTPP with the Cu atoms resulting in the specific orientation and direction of diffusion. *e), f)* STM micrograph of 2HTPP/CoTPP mixture on Cu(111) ($U = -1.35$ V, $I = 30$ pA) and corresponding average image of subsequently acquired STM data (26 frames, ~ 21 min total). The island exhibits square order and consists of CoTPP, while the isolated molecules are 2HTPP.

Here a mixture of the latter molecules was evaporated onto the Cu substrate resulting in CoTPP islands with the molecules arranged in the square order coexisting with isolated 2HTPP more or less randomly scattered on the surface. The average image of a corresponding STM time series evidences the demobilization of the molecules within the CoTPP island, whereas analyzing all frames the continuous appearance and disappearance of individual molecules at the border of the ordered island is observed. As mentioned above this is in accordance with the condensation of the island from a 2D-gas, i.e., from fast moving CoTPP molecules [70]. The 2HTPPs are diffusing along the main crystallographic directions as known from the system without coadsorbed CoTPP (see above). From a general standpoint this example is especially valuable and unique since it directly illustrates how variations in the molecular theme (here metalation) can switch the adsorption behavior from domination of molecule/substrate (here 2HTPP) to molecule/molecule interactions (here CoTPP); in addition a separation of the two molecular species is realized.

The last example to be discussed in this subchapter is the self-assembly of CoTTBPP on Ag(111). For comparison it is important to realize that the latter molecule is practically a CoTPP with tert-butyl attached to the 3 and 5 positions of the phenyl rings, i.e., a variation in the peripheral substituents. A succinct comparison of ordered arrays of CoTPP and CoTTBPP can be found in [P7], an in-depth investigation of the self-assembly of CoTTBPP on Ag (111) is given in [P3]. In the latter work three coexisting clearly distinguishable ordered phases of CoTTBPP were observed after deposition with the sample held at room temperature. A high resolution STM image of one of these arrangements namely a square arrangement with a lattice constant of 1.60 ± 0.06 nm is shown in Figure 2.8 a and with the corresponding overlaid models in 2.8 b (see [P3] for the description of other two arrangements). The overall appearance of an corresponding individual molecule in STM at the given tunneling conditions is dominated by the four upper tert-butyl groups forming a rectangle as indicated by the aligned model in Figure 2.8 d. Choosing a different preparation route, namely the thermal desorption of an excess multilayer molecules of beforehand deposited CoTPP, one observes a novel, extremely rigid herringbone structure. The supramolecular assembly and intramolecular conformation is depicted in Figure 2.8 e-h, partially with the adjusted models.

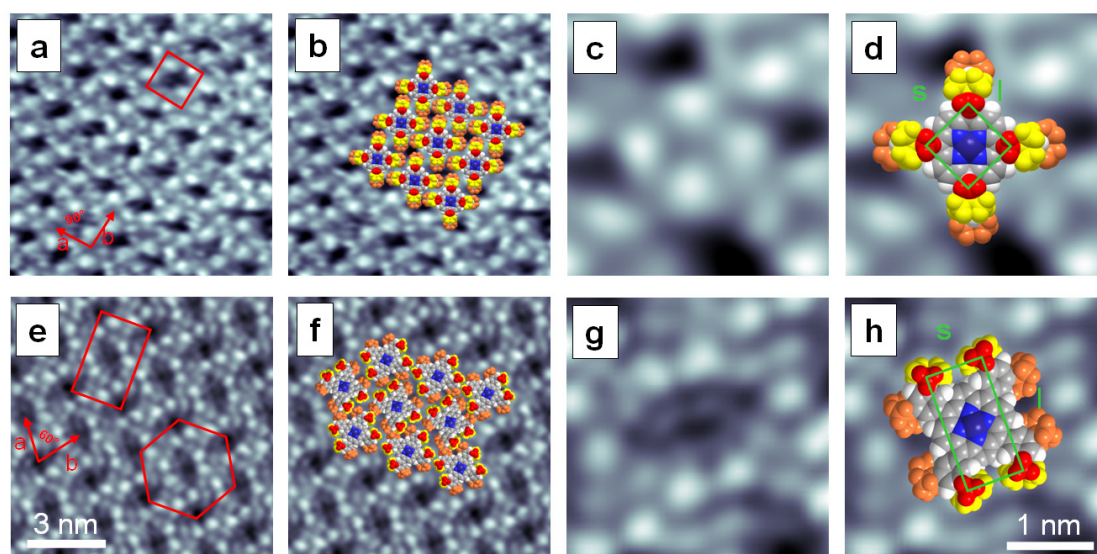


Figure 2.8 Overview of STM images of two selected out of four phases observed in CoTTBPP on Ag(111) with and without the corresponding molecular models superimposed: (a-d) square phase, (e-h) herringbone phase. The size of the STM images is (10×10) nm² for the first two columns and (3×3) nm² for the remaining. The molecular models are scaled to fit and placed by hand in the STM images. The tunneling parameters are for (a-d) $U_{Gap} = 1.30$ V, $I_{Set} = 0.30$ nA, (e-h) $U_{Gap} = 1.17$ V, $I_{Set} = 0.36$ nA. The figure is adapted from [P3]

To understand the obvious differences in the arrangement and intramolecular conformation one has to consider the known flexibility of the di-tert-butyl-phenyl (DBP) ligands [9, 71, 86-88]. In single molecule experiments performed by Moresco et al., the STM tip was used at ~15 K to laterally manipulate the very similar CuTTBPP on Cu(211) and Cu(100) [87, 88]. It was found that the dihedral angle between the DBP ligands (with the attached tert-butyl groups) and the porphyrin plane changes upon lateral manipulation, demonstrating the ability of the large molecule to conformationally adapt to the surface topography. A similar effect had already been described in 1997 in a milestone work by Jung et al., who reported that the overall supramolecular self-assembly and the intramolecular conformation of CuTTBPP depends on the actual substrate (Cu(100), Au(110), Au(110), and Ag(110)) [9]. The authors describe the deformation of individual CuTTBPP molecules by an antisymmetric rotation of two opposite DBP substituents as a result of the delicate balance of an attractive molecule-substrate interaction and the steric repulsion between the ortho-substituents. In other words, molecule/substrate interactions account for the structural variations in the CuTTBPP adsorbed on different surfaces. Observing three different coexisting phases for CoTTBPP it becomes apparent that also molecule/molecule interactions have to be considered for the intramolecular deformations, at least for the specific system. To achieve a consistent picture of the deformations of individual molecules in STM, an additional tilt angle of the DBP substituents had to be introduced in [71, 89] [P3]. Based on the perimeter (mainly influenced by the tilt angle) and the aspect ratio (mainly determined by the dihedral angle, i.e., the DBP rotation out of the porphyrin plain) of the rectangles formed by the upper tert-butyl groups, the corresponding deformation of CoTTBPP could be estimated. The largest deformation in terms of the dihedral angle was observed for the herringbone arrangement with 20°, i.e., with the phenyl in DBP almost parallel to the porphyrin plain. As a result also the lower tert-butyl groups are visible in Figure 2.8 g as dim protrusions and the macrocycle significantly approached the surface. The estimated surface/macrocycle distance (center Ag-center Co) can be estimated to be roughly 0.5 nm. Thus the original idea to increase the surface/metal distance in comparison to CoTPP by the substitution of the phenyl groups with the comparably bulkier DBP substituents apparently fails. On the other hand the discussed overall conformation and arrangement of the herringbone phase proved to be extremely stable due to the strong interwoven character of the particular molecular order and can thus be suggested as a motif for a functional molecular architecture [P3].

The diversity of structures demonstrates that the interactions that finally lead to the formation of self-assembled arrays of tetrapyrroles are complex and depend on various parameters, e.g., the tuning of the porphyrin-substrate distance by the

attachment of different substituents as proposed in Figure 2.3 proved to be inoperative, at least for the system studied here.

2.2 In situ metalation of free base porphyrins and phthalocyanines

In the context of the work at hand the possibility to directly metalate free-base tetrapyrroles in UHV by coadsorption or predeposition of metal atoms was explored and a detailed understanding of the underlying processes could be achieved. Corresponding in situ coordination reaction could be demonstrated for Fe [79, 90] [P1, P5, P6, P8, P10], Co [62] [P2, P7], Zn [61], Ce [57] and Ni [83]. The in situ metalation is especially advantageous in the case of compounds undergoing chemical modifications under ambient conditions. As a prototype example iron porphyrins are very sensitive towards oxidation and thus difficult to handle and to sublime as a pure compound. Another advantage is the controlled functionalization of porphyrins upon metalation depending on the actual metal.

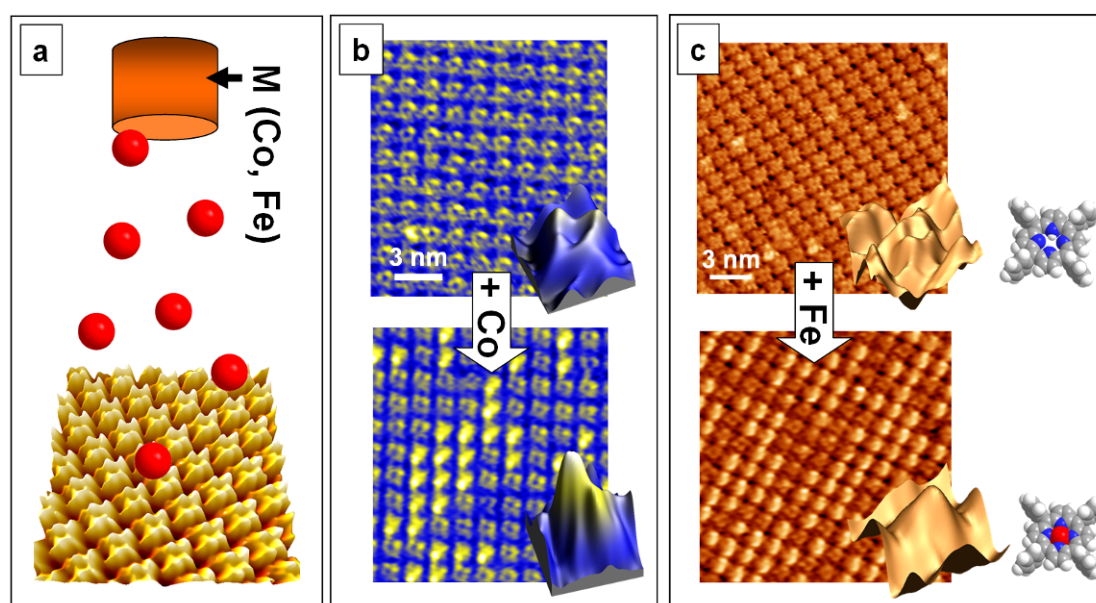
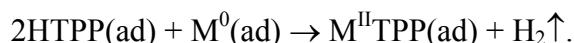


Figure 2.9 a) Sketch of the direct metalation by in situ evaporation of metal atoms onto a monolayer 2HTPP on Ag(111). The image at the bottom is a 3D plot of corresponding STM data. b), c) STM data proving the in situ metalation reaction of 2HTPP to CoTPP and FeTPP, respectively. While the individual 2HTPP molecules appear with a central depression the corresponding metalloporphyrins appear with increased apparent height, in the larger images as well as in the extracted 3D plots of selected individual porphyrins. The STM data is adapted from [P2]/b) and from [P1]/c).

Figure 2.9 illustrates the method and selected STM results of the metalation of 2HTPP with Co respective Fe on Ag(111) by evaporation of the corresponding metals onto an ordered monolayer of the free-base porphyrin. The metalation reaction proceeds via an initial complex followed by the release of pyrrolic hydrogen as H₂, given by the equation [P2, P7]:



For the given examples (Fe, Co) the reaction proceeds at RT, whereas for Zn an activation barrier has to be overcome, i.e., heating of the sample is required [61]. In STM the changed appearance of individual molecules provides indirect evidence for the metalation reaction as illustrated in Figure 2.9. Therefore the combination with spectroscopic information provided by XPS from the group of Michael Gottfried (Erlangen) proved to be especially valuable to consolidate the information of the chemical processes in the course of the metalation [62] [P2, P5, P6, P7]. Remarkably, the yield for the metalation of a monolayer 2HTPP with Fe and Co on Ag(111) was found to be close to 100%. A sequence of STM images of a TPP monolayer with incremental increasing Fe dose is depicted in Figure 2.10. The FeTPP molecules appear as protrusions in the square molecular arrangement. In Figure 2.10 a-d the amount of Fe dosed onto the 2HTPP monolayer is successively increased by one third of the stoichiometric amount needed to metalate all free-base porphyrins. Statistics over larger areas within this experimental run resulted in a maximal metalation degree of 89%, whereas the metalation grade for the first two steps was estimated to be 29% and 60%, i.e., approximately 100% yield [P1]. From these numbers one gains further insight into the specific metalation process.

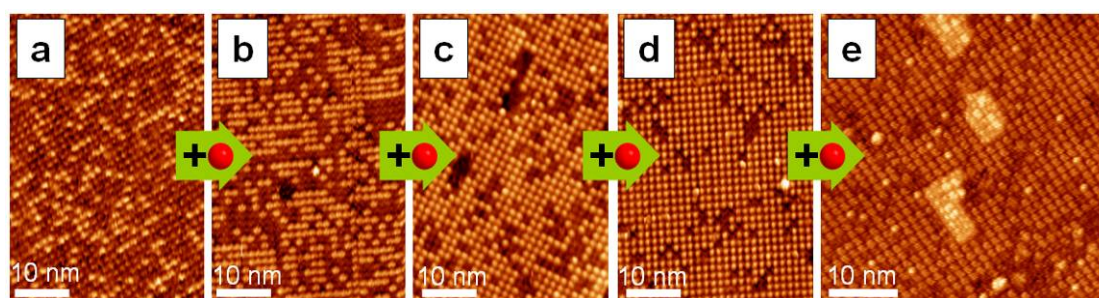


Figure 2.10 a)-d) STM micrographs of successive deposition of a Fe portion corresponding to 1/3 of the stoichiometric amount needed to metalate one monolayer 2HTPP. The corresponding metalation grades were estimated to a) 29%, b) 60%, c) 73% and d) 89%. **e)** The metalated porphyrin layer after excess Fe deposition. The area of the island reflects roughly the amount of excess Fe. The Figure is adapted from [P1].

Considering the impinging of the Fe atoms as a random process, i.e., not directed to the center of the molecules it is clear that most of the atoms first adsorb on the surface and then diffuse to the molecular coordination site. In other words: the metalation process is surface mediated. Upon excess dosage of Fe, as shown in Figure 2.10 e, islands start to form [P1, P8]. The formation of these structures is in line with the formation of Fe-islands directly on the Ag surface, i.e. underneath the porphyrin macrocycles. Therefore, one might assume that the distance in between the porphyrin macrocycle of the TPP species and the Ag(111) surface is necessary to allow diffusion of the metal atoms. However, the same metalation approach with tetrapyrrolic species, where the porphyrin plane is in close proximity to the substrate resulted in very similar findings, in particular metalation yields close to 100%. Examples are the metalation of 2HOEP on Cu(111) with nickel to NiOEP [83] and on Ag(111) with iron to FeOEP [91]. In [P5] the metalation of 2HPc on Ag(111) with Fe to FePc is reported in detail, another example for a tetrapyrrolic species, where the macrocycle is in direct contact to the substrate. These three examples clearly demonstrate that the diffusion of the corresponding metals does not rely on a significant gap between the tetrapyrrolic plane and the surface. In addition the metalation of 2HPc close to 100% yield evidences that no side reactions with the peripheral nitrogen atoms of the phtalocyanine occurs. To further investigate the diffusion of iron on a Ag(111) surface in presence of a closed layer of TPP or Pc a comparative STM study was conducted in [P8]. First the epitaxial growth of iron on Cu(111) was observed. It was found that for low coverage iron tends to form small 3D island at the step edges as shown in Figure 2.11 a. Since the island formation process relies on the mobility of Fe to the nucleation sites, one concludes that the diffusion length exceeds the terrace width [68, 69]. Upon increasing iron coverage 3D islands also tend to form on the terraces. In respect to the large lattice mismatch of Fe with Ag the observation is in agreement with observations in other metal/metal systems with large mismatches [92-95]. As evident from Figure 2.10 e the growth of iron is considerably modified by the presence of a TPP layer. In comparison to the predominant modified growth in islands growing with coverage underneath the TPP layer, the Fe growth with the preadsorbed Pc layer is dominated by a large number of small 3D clusters apparently between the molecules. In classical metal/metal epitaxy the growth of a larger amount of smaller clusters can be explained by reduced mobility (lower sample temperature [93-95]). Applied to the tetrapyrrole modified surfaces this would mean that Fe experiences reduced mobility on the Pc covered surface, which is in line with the argument concerning the smaller gap between the macrocycle and the surface. In a simple picture the cavity in between the TPP core and the substrate enables the Fe atoms to diffuse more freely in that gap underneath

the porphyrin ring. But also the peripheral nitrogen atoms of the Pc might contribute to the observed growth mode. Even though more efforts have to be made to clarify the nature of the effect it is evident that preadsorbed layers of tetrapyrrolic derivatives modify the growth of Fe on Ag(111) and presumably in other metal/metal systems and thus establish a novel way to influence the growth of metal clusters.

Further information can be extracted from an experiment with a reversed order of the “ingredients”, i.e., starting with a Ag(111) surface covered with a certain amount of Fe as depicted in Figure 2.11 a. In the next step a monolayer 2HTPP is evaporated onto the Fe precovered surface [P6]. An STM micrograph of the situation is shown in Figure 2.11 b. Apparently the Fe clusters are stable at room temperature even after several days, indicating that the Fe atoms are pinned to the clusters. After heating the sample to 550 K a certain fraction of the molecules appears as protrusions. The number of these protrusions correspond to the stoichiometric amount of deposited Fe and can be identified with FeTPP. This can be interpreted such that the metalation is energetically favorable but kinetically hindered by the prior cluster formation. Revisiting the system 2HTPP on Cu(111) it can be speculated that the specific molecule/substrate interaction is due to the coordination of the pyrrolic nitrogen to the substrate atoms, forming a precursor state of the metalation with Cu.

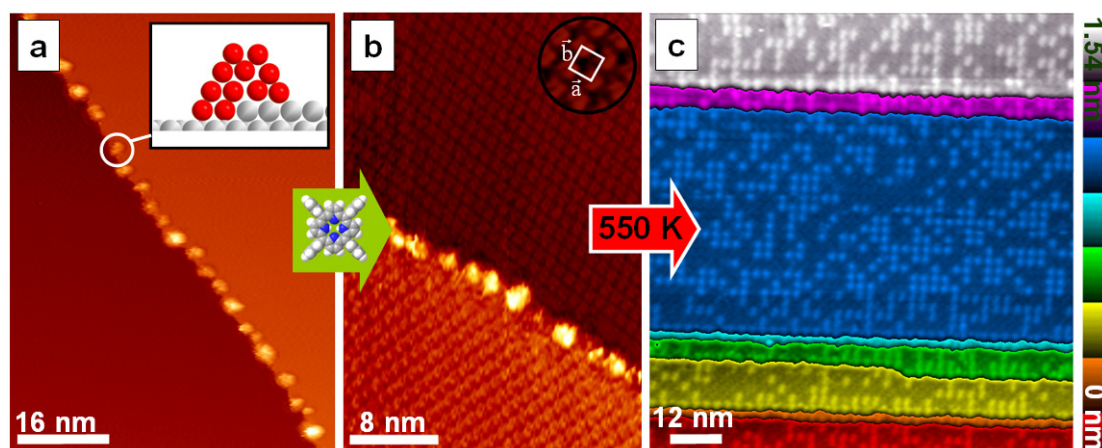


Figure 2.11 In situ metalation of 2HTPP with preadsorbed Fe via thermal activation. **a)** STM image showing the nucleation of 3D Fe clusters on step edges of Ag(111). 0.025 ML of Fe were deposited at room temperature ($I = 35 \text{ pA}$; $U = -1.2 \text{ V}$). **b)** 2HTPP monolayer prepared via vapor deposition onto the surface depicted in **a)** ($I = 24 \text{ pA}$; $U = 0.45 \text{ V}$). The image shows an ordered 2HTPP monolayer at the terraces coexisting with iron clusters at the step edges. **c)** Situation after heating the surface shown in Figure **b)** to 550 K (terraces individually color-coded). The bright spots in **c)** are assigned to FeTPP formed by metalation of 2HTPP ($I = 37 \text{ pA}$; -1.57 V). Figure and caption adapted from [P6].

In this regard it is important to mention that 2HOEP does not exhibit the reduced mobility on Cu(111) as observed for 2HTPP. One of the main differences of the two species is that 2HOEP adsorbs in a flat geometry without significant deformation of the macrocycle [P9], whereas 2HTPP undergoes a certain deformation sketched in Figure 2.7 c [13, 57, 71] [P6-P9]. As a result the nitrogen atoms of 2HTPP point towards the Cu surface which might explain an enhanced coordination and thus interaction. Regarding the successful in situ metalation in various systems studied in this thesis and other publications so far [57, 79, 90] it is suggested that the reaction is of general nature and should be expandable to other porphyrin / metal combinations.

Table 2.1 Listing of the surface mediated metalation reactions proved to be effective in this thesis.

free-base tetrapyrrole	complexed metal	Substrate	sample temperature	references
2HPc	Fe	Ag(111)	RT	P5
2HOEP	Fe	Ag(111)	RT	[91]
2HTPP	Fe	Ag(111)	RT; 550 K for predepos. Fe	P1, P8, P10
2HTPP	Co	Ag(111)	RT	P2, P7
2HTPP	Ni	Cu(111)	RT	[83]
2HTTBPP	Fe	Ag(111)	RT	[74]

2.3 Spectromicroscopic investigations and electronic structure

Up to this point the appearance of the investigated porphyrinoids in STM was mainly discussed as a result of the topography of the molecules. This intuitive approach is in many cases (e.g., the ones discussed up to this point) sufficient to explain the apparent shape in STM. However it is clear that the electronic states of the tip and the sample also contribute to the corresponding apparent height in STM. Generally the appearance in STM is an interplay of the electronic structure and the topography of the imaged object. In a constant current STM micrograph all electronic states from the bias voltage to the Fermi energy contribute to the tunneling current and thus to the apparent height in the micrograph. Therefore, by the variation of the offset voltage one gains information of the electronic structure or more specifically of the local density of states. Depending on the polarity the information concerns the highest

occupied (negative polarity) or the lowest unoccupied states. A first example concerns polarity dependent appearance of CoTTBPP. In Figure 2.12 b the molecular arrangement and in the blow-up the appearance of an individual molecule are depicted at positive bias voltage. Here the four prominent bright spots reflect the position of the highest butyl groups, as discussed above in the context of Figure 2.8 and in [9]. The central depression at the position of the complexed Co ion obviously does not reflect the topography in contrast to the periphery of the molecule. Therefore, it is concluded that the local density of states at the center is small or, in other words, that there is no or no pronounced (lowest) unoccupied molecular orbital (LUMO). In distinction the images in Figure 2.12 a are acquired at negative bias showing a pronounced central protrusion, which dominates the appearance of the molecule in STM at the given conditions [74]. Obviously the apparent height of the central Co in the micrograph is exaggerated in comparison to the actual topography of the molecule. This indicates a pronounced electronic state, i.e., the highest occupied molecular orbital (HOMO) in between -0.8 eV and the Fermi edge. Indeed, Lukasczyk et al. reported an corresponding electronic state of CoTTBPP on Ag(111) at ~ -0.7 eV by means of ultraviolet photoelectron spectroscopy (UPS) [56]. Since UPS is restricted to HOMO states one might gain additional information from STM measurements in which also the LUMO states are accessible. It can be noted that in the specific case studied here the intramolecular appearance of the CoTTBPP molecules changes significantly upon polarity change of the bias voltage.

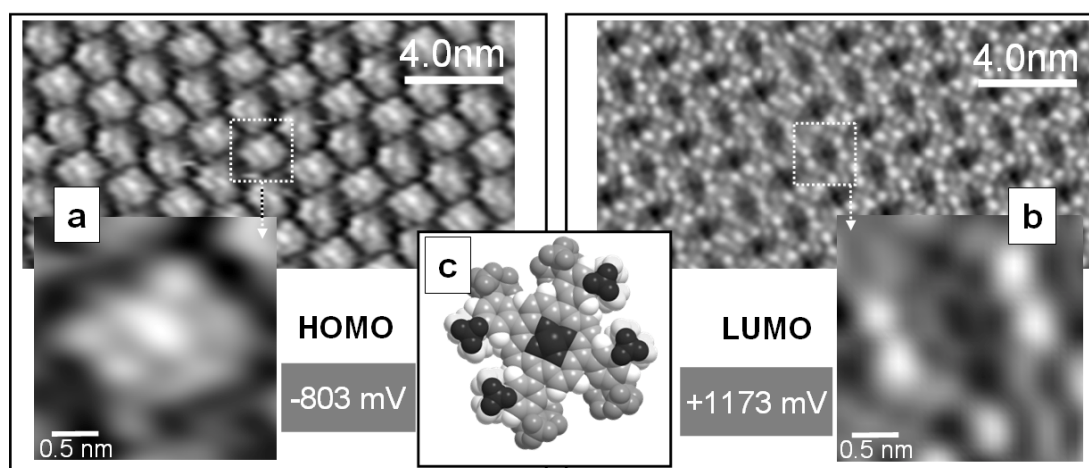


Figure 2.12 Constant current STM micrographs of a CoTTBPP monolayer in herringbone arrangement recorded with **a)** $I_{set} = 44$ pA, $U_{gap} = -803$ mV and **b)** $I_{set} = 36$ pA, $U_{gap} = +1170$ mV. **C)** Scaled model of the CoTTBPP in the herringbone structure (compare Figure 2.8 and [P3]). Figure adapted from [74].

Even though the findings discussed so far include some indirect information of the LDOS of the adsorbed molecule it is also possible to acquire more specific data via scanning tunneling spectroscopy (STS) [96, 97]. In this technique, variation of the tunneling current with increasing and/or decreasing bias voltage is recorded. This can be done in different ways. The most prominent is the acquisition of local ST spectra; however, in this method one has to rely on very good position stability of the instrument and therefore this type of local spectroscopy is mostly performed in low temperature STMs. In the RT experiments conducted in the framework of the thesis at hand a special technique had to be employed, namely the continuous imaging spectroscopy mode (CITS) [97, 98]. In CITS the STM follows a constant current contour, acquiring an ST spectrum at each point. In this way a data set can be recorded in which each ST spectrum is assigned to a point of a constant current STM image. The CITS data can then be processed in different ways, e.g., as dI/dV maps directly relating to the LDOS [74] or by averaging spectra high quality STS data can be extracted. In the following an example for the latter will be discussed in regard to a contrast inversion in STM images of a mixed CoTPP/2HTPP monolayer on Ag(111) [P4]. Figure 2.13 b shows a medium resolution STM image of a CoTPP/2HTPP mixture with a ratio of roughly 9:1 on Ag(111). The image contrast is the same as discussed in chapter 2.2, used to evaluate the data in terms of metalation grade, i.e., the metalloporphyrins appear brighter than the free-base TPP.

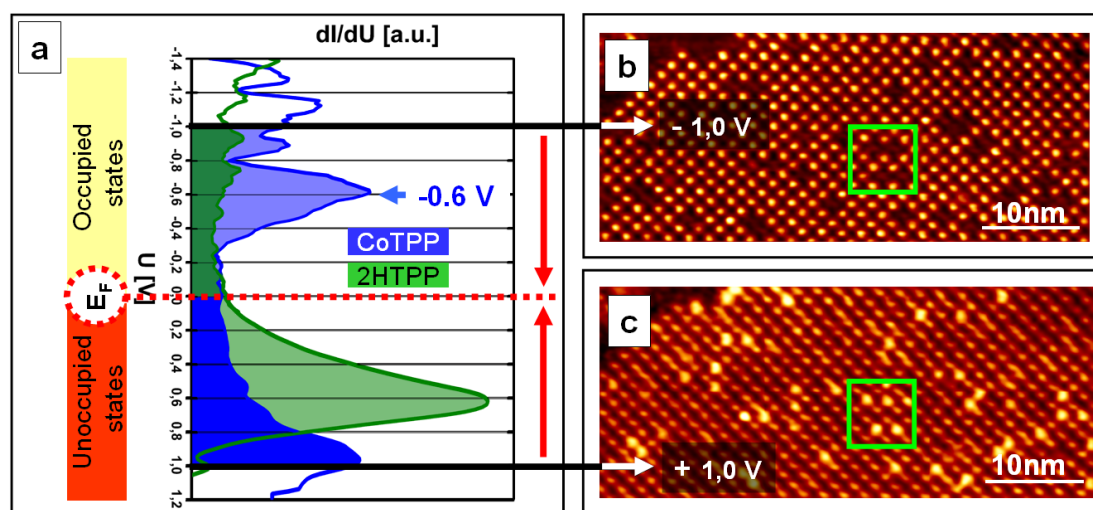


Figure 2.13 a) Local ST spectra reflecting the LDOS of CoTPP (blue line) and 2HTPP (green line) are plotted. The ST spectra were extracted from CITS data of a mixed layer of CoTPP and 2HTPP. b), c) Constant current STM images (both with $I_{set} = 0.27$ nA) of a monolayer CoTPP on Ag (111), in b) at negative bias voltage -1 V and in c) at positive bias voltage $+1$ V. The apparent contrast inversion can be recognized by direct comparison of the green rectangles in b) and c). Figure and caption adapted from [P4].

However, a polarity switch of the bias voltage from -1 V to +1 V results in a contrast inversion, i.e., the 2HTPP appear brighter in Figure 2.13 (note green box). The corresponding tunneling spectra acquired for CoTPP (bluish) and for 2HTPP (greenish) enable to gain deeper insight into the electronic structure of the adsorbed porphyrins. Whereas the contrast for negative bias is dominated by a prominent state at -0.6 V of the CoTPP [56], the positive bias region from +1 V to the Fermi energy an electronic state from the 2HTPP surmounts the CoTPP states. Considering the contribution of the corresponding states the origin of the observed contrast inversion becomes clear and is discussed in detail in [P4]. The existence and origin of the HOMO peak at -0.6 eV was well investigated via UPS by the group of Michael Gottfried [56, 99] [P4, P7], where the state was indentified as a interaction peak of the CoTPP or more specifically the half filled d_z^2 orbital of the central Co ion with the Ag(111) surface. Considering the shape of the corresponding orbital one would expect that it appears as a central bright spot in STM. However, the intramolecular shape of different adsorbed metallo-TPP molecules in STM with negative bias voltages was described with the elongated shape discussed above in context with Figure 2.6 [13, 57, 71] [P6-P9] and also shown in 2.14 a, b. In [P10] we were able to demonstrate that CoTPP on Ag(111) indeed appears as a centered spot at bias voltages closer to the Fermi edge, i.e., at bias voltages starting from -0.4 V as depicted in Figure 2.14 d, e [P10]. This bias dependent appearance also enabled to discriminate the chemically very similar CoTPP from FeTPP. This is especially remarkable since Fe and Co complexed in a tetrapyrrolic environment are assumed to both have a half filled d_z^2 , which is assumed to provide a dominating tunneling channel [14, 100]. For this reason FePc and CoPc are predicted to be undistinguishable in STM [101]. Detailed insight of the observed peculiar appearance could be achieved by density functional theory (DFT) based simulations of the adsorbate complex by the group of Andreas Görling and Wolfgang Hieringer in the framework of the SFB 583. In the corresponding calculations the experimentally observed appearances of 2HTPP, FeTPP and CoTPP (Figure 2.14 f) were reproduced via periodic density-functional calculations [102-104] and applying the Tersoff-Hamann model [105, 106]. The nature of the bias dependent shape of CoTPP could be traced back to an particular orbital of the adsorbate complex with pronounced d_z^2 character as depicted in side view in Figure 2.14 g. Even though in some cases simpler approaches, such as extended Hückel Theory calculations might reproduce the main features observed in STM [11, 13, 79, 107] in others also sophisticated calculations neglecting the surface do not lead to satisfying agreement [108].

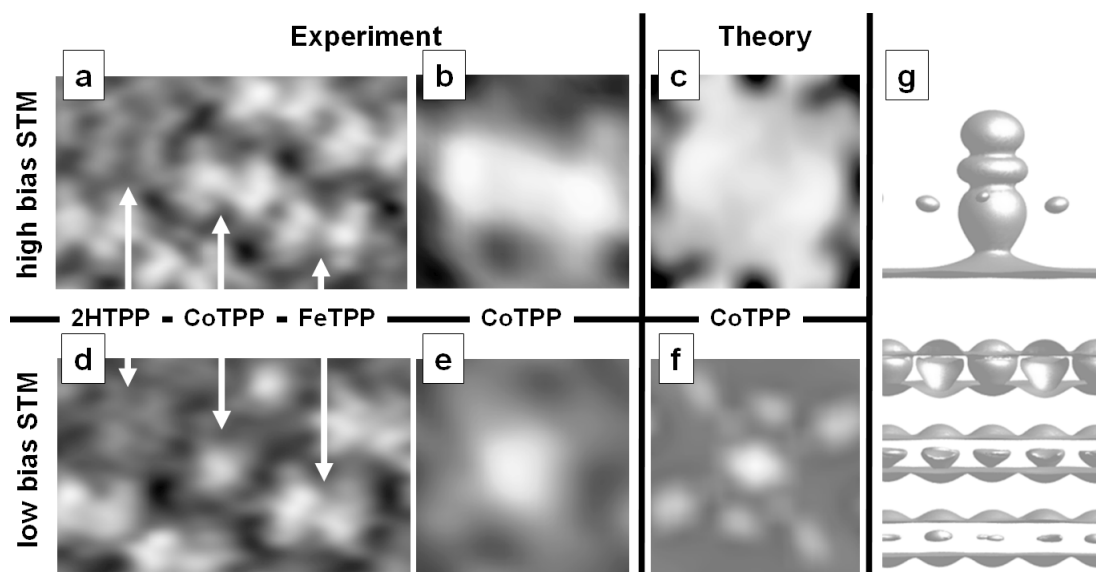


Figure 2.14 a), b), c), d) Experimental Constant current STM images of the indicated TPP molecules acquired at high negative bias in a) $I_{set} = 30 \text{ pA}$, $U_{gap} = -810 \text{ mV}$, b) $I_{set} = 35 \text{ pA}$, $U_{gap} = -1200 \text{ mV}$ and at low negative bias in d), e) $I_{set} = 35 \text{ pA}$, $U_{gap} = -240 \text{ mV}$. c), f) Corresponding simulated STM images calculated for $U_{gap} = -200 \text{ mV}$ (low bias) and $U_{gap} = -1030 \text{ mV}$ (high bias). f) Side view of orbital density of highest occupied orbital in the Ag(111)/CoTPP adsorbate system. The Figure is adapted from [P10].

For the simulation discussed above comparison with gas phase calculations demonstrated that the surface plays an active role and has to be taken into account to reproduce the low bias results for CoTPP. The shape of 2HTPP with a central protrusion and the saddle-shape for FeTPP molecules on Ag(111) and at negative bias voltages could be assigned to orbitals closely resembling the topography of the molecules. In addition the rotation of the phenyl rings $\sim 60^\circ$ out of the porphyrin plane could be confirmed by the calculations as a precondition to reproduce the experimental findings.

2.4 Coadsorption of small molecules

Besides the choice of the peripheral substituents and the substrate or the preparation route for the generation of specific arrangements of large organic molecules also the coadsorption of other organic molecules often leads to the formation of well-ordered mixed layers [109-114]. As a novel aspect of the work at hand the influence of coadsorbed small molecules on the supramolecular order of porphyrin arrays was explored. In [P11] the massive rearrangement of initially square ordered CoTPP molecules upon coadsorption of NO at RT is reported.

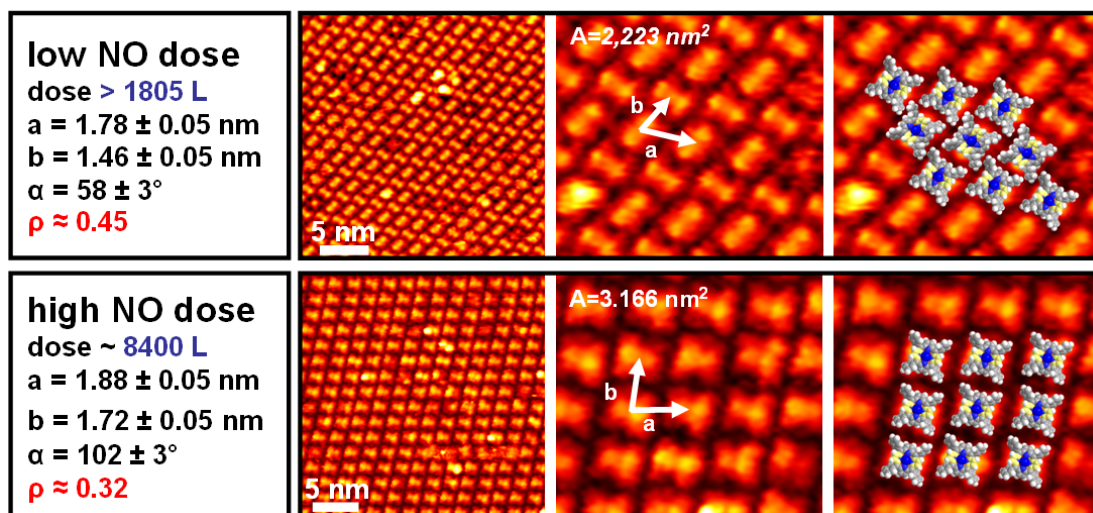


Figure 2.15 STM micrographs of two ordered arrangements of CoTPP on Ag(111) after dosage of the indicated NO dose. The tunneling parameters for the upper row are $U_{gap} = -1.9$ V, $I_{set} = 45$ pA and for the bottom row $U_{gap} = -1.9$ V, $I_{set} = 45$ pA.

In Figure 2.15 STM images of two out of at least eight ordered structures after NO dosing are depicted. On a first glance the deviations from the “native” square order can be discriminated, e.g., in both cases the azimuthal orientation of the CoTPP in the supramolecular arrangement changed upon NO dosing. Another important observation is the decreasing molecular density of the CoTPP on Ag(111) with increasing NO dose. This would be in line with a coadsorption of NO between the porphyrins.

Indeed XPS data by the group of Michael Gottfried (Erlangen) and LT STM data from the group of Johannes Barth and Wilhelm Auwärter (TU Munich) evidenced the coadsorption and even revealed the positions of the NO in the rearranged CoTPP phase [P11]. The overall energy minimization is proposed to be due to dipole-dipole interactions. The presumably general nature of the rearrangement process is also indicated by similar observations in the Systems NO/2HTPP/Ag(111) and CO/FeTPP/Ag(111) [115]. Besides the potential to use the coadsorption of small molecules as a tool to control the ordering in UHV one also has to consider similar effects quite generally in the production of functional layers from large organic molecules under ambient conditions or after exposure to small electronegative molecules.

A different approach to influence the arrangement of porphyrins on a Cu(111) surface was to generate monoatomic oxygen islands by dosing oxygen at room temperature and then to evaporate different TPP molecules onto the oxygen modified surface. Figure 2.16 summarizes the main findings.

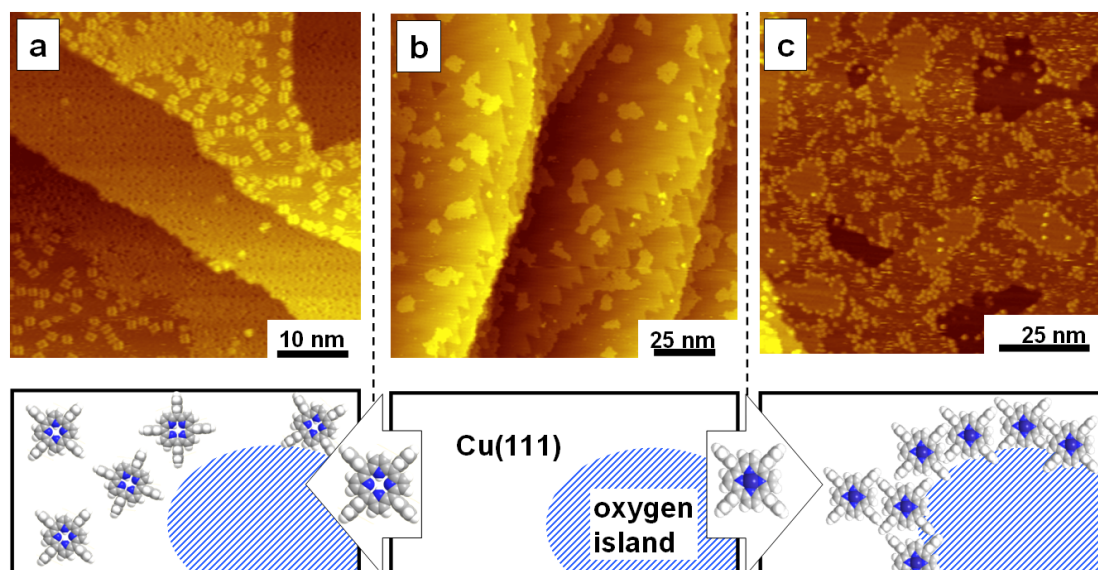


Figure 2.16 STM micrographs with corresponding sketches illustrating the adsorption of **a)** 2HTPP and **c)** CoTPP on a Cu(111) surface precovered with oxygen islands as shown in **b)**. The tunneling parameters are: **a)** $U_{gap} = -1.01$ V, $I_{set} = 21$ pA, **b)** $U_{gap} = -1.66$ V, $I_{set} = 40$ p, **c)** $U_{gap} = -1.14$ V, $I_{set} = 30$ pA.

It was found that 2HTPP selectively occupies the surface areas free of oxygen, whereas CoTPP is pinned to the rim of the islands. These findings indicate the possibility to pattern a surface with porphyrins by a given template, here the oxygen islands.

2.5 Summary and current research activities

The intramolecular conformation and supramolecular ordering of OEP, TPP and TTBP molecules was studied in detail. Thereby a deeper understanding of porphyrins adsorbed on metal surfaces could be achieved. As a consequence, different approaches to tailor the two dimensional porphyrin architectures were applied; these include conventional concepts like the attachment of different peripheral substituents to the macrocycle or the substrate dependence of the adsorption properties, but also novel aspects like the in situ metalation and the coadsorption of NO with CoTPP, which induces a sequence of ordered structures. An additional new approach to influence the arrangement of porphyrins on a Cu(111) surface was to generate monoatomic oxygen islands by dosing oxygen at room temperature and then to evaporate different TPP molecules onto the oxygen modified surface. It was found, that the assembly of TPP molecules correlates to the given oxygen template.

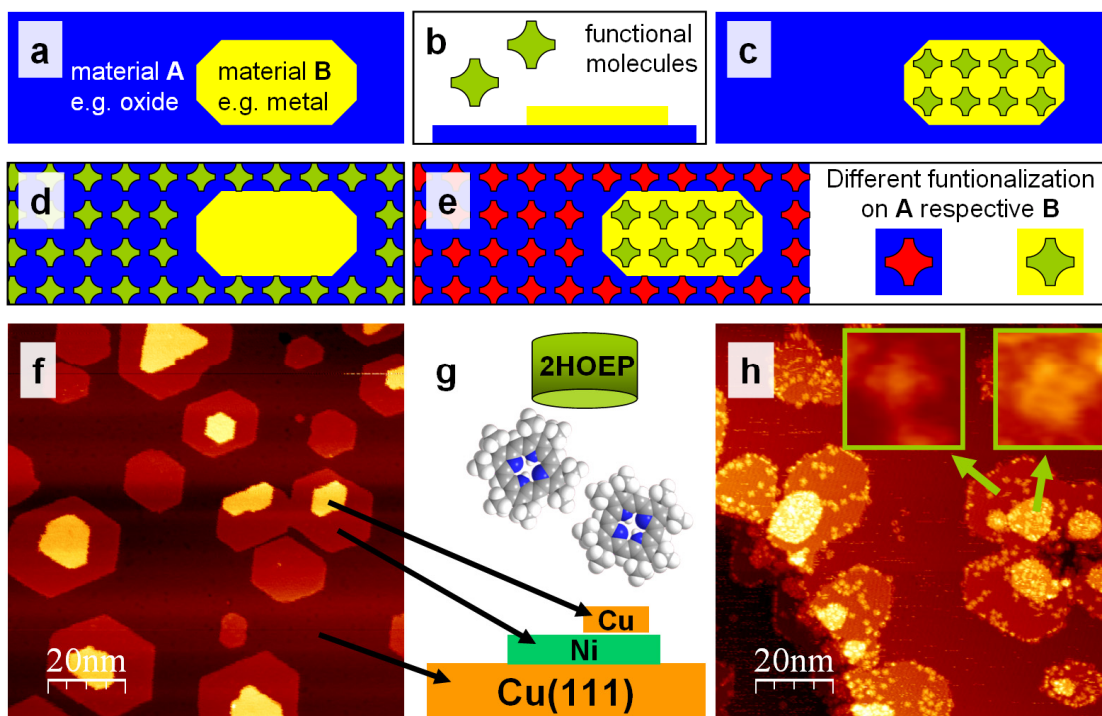


Figure 2.17 a)-e) Sketch of the simplified concept to direct the assembly of porphyrins on a surface. **a)** Prestructured surface. **b)** Evaporation of functional molecules onto the template shown in **a)**. **c)-e)** Different scenarios of selective anchoring or functionalization of the molecules depending on the local substrate **f)** Constant current STM image of Ni islands on Cu(111) and of Cu on Ni islands on Cu(111). **g)** Scheme of the evaporation of 2H-octaethylporphyrin on the composite surface shown in **f)**. **h)** Constant current STM image of the composite surface shown in **f)** after evaporation of a small amount of 2HOEP. In addition to the obvious agglomeration of the porphyrins on the two islands types the insets in **h)** also indicate that 2HOEP is selectively metalated on the Ni islands[83].

This observation indicates a strategy to generate templates for the adsorption of functional molecules to realize patterning via local anchoring. Based on the findings concerning the substrate influence (e.g. reduced mobility of 2HTPP on Cu(111) in comparison to Ag(111)) this concept can be expanded to, e.g., composite metallic surfaces. Indeed we successfully tested this idea on a Cu(111) surface prestructured with Ni islands. For TPP molecules selective anchoring on top of the Ni islands was observed (not shown here). Interestingly for the system 2HOEP on Ni/Cu(111) in addition to the anchoring also indications for a selective metalation of the free base porphyrin with Ni on the Ni islands was found as depicted in Figure 2.17 h [83]. The exploration of the strategy illustrated in Figure 2.17 a-e is in the focus of currently running and future experiments. A possible concept of how to generate corresponding templates can be found in chapter 3 based on focused electron beam induced processing.

The second main aspect concerns the investigations of the electronic structure of the porphyrin/metal adsorbate complexes. It was demonstrated that it is crucial to gain information of the LDOS to correctly interpret the constant current STM data, as illustrated by the contrast inversion of an intermixed 2HTPP / CoTPP layer upon polarity change of the bias voltage. The detailed combined theoretical and experimental investigation in particular of CoTPP on Ag(111) shed some light on the long discussed role

3 Fabrication and characterization of nanostructures by means of a highly focused electron beam [P12-P16]

On a microscopic level the chemical properties of atoms or molecules are determined by the electron configuration. Therefore, the injection or removal of electrons can be a suitable tool to trigger chemical processes, like bond formation or dissociation. Thus electrons can be regarded as an excellent tool to modify or engineer the properties of different materials [116-119]. The long mean free path and the availability of electron sources in high vacuum (HV) or UHV chambers makes this environment especially suitable to study electron induced processes. Numerous publications investigate the macroscopic electron induced modification of molecules adsorbed on well defined surfaces [120-124]. One of the main effects reported is the electron induced bond scission, leading to the dissociation of adsorbed molecules. But also the electron stimulated desorption (ESD) was studied in detail; by the technique of electron stimulated desorption ion angular distribution (ESDIAD) even conclusions on the orientation of chemical bonds could be derived [123]. With the advent of extremely small electron probes available in SEM, TEM and STM it became possible to spatially confine the impact of the electrons [20, 28, 125, 126]. This is exploited in the technique of electron-beam induced deposition (EBID) in which a highly focused electron beam from an SEM or TEM is used to locally crack, e.g., metal containing precursor molecules, resulting in the deposition of the non-volatile fragments [20-23, 28, 127]. The ideal EBID process is sketched in Figure 3.1.

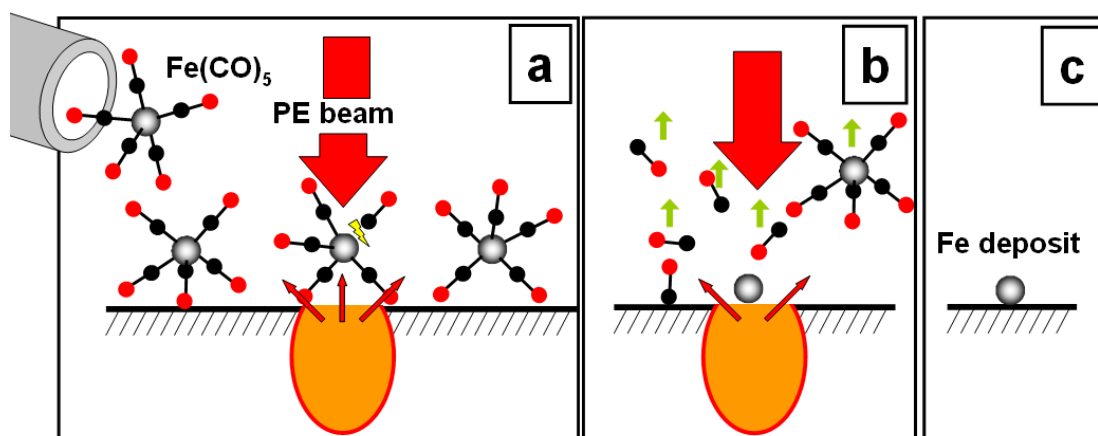


Figure 3.1 Sketch of the ideal EBID process with the precursor molecule $\text{Fe}(\text{CO})_5$. **a)** Dosage and adsorption of the precursor molecule $\text{Fe}(\text{CO})_5$ during local irradiation of adsorbed molecules to the primary electron-beam and resulting secondary electrons. **b)** Decomposition of the $\text{Fe}(\text{CO})_5$ molecule exposed to electrons and desorption of the volatile fragments (e.g., CO) and the unexposed $\text{Fe}(\text{CO})_5$. **c)** Pure iron deposit at the electron exposed position after the EBID process.

Two main goals for EBID as a tool to engineer nanostructures can be immediately formulated:

- i) **controlled shape and size**, i.e., small deposits
- ii) **defined chemical composition**, i.e., clean deposits

Concerning point i), lithographic attachments enable to control the path of a focused electron beam on the substrate and thus to target arbitrary shapes of the EBID deposits. However, size and shape of the deposited structures is limited by so-called proximity effects, i.e., the effective broadening of the electron beam in the substrate due to secondary effects [21, 22, 29, 127-136].

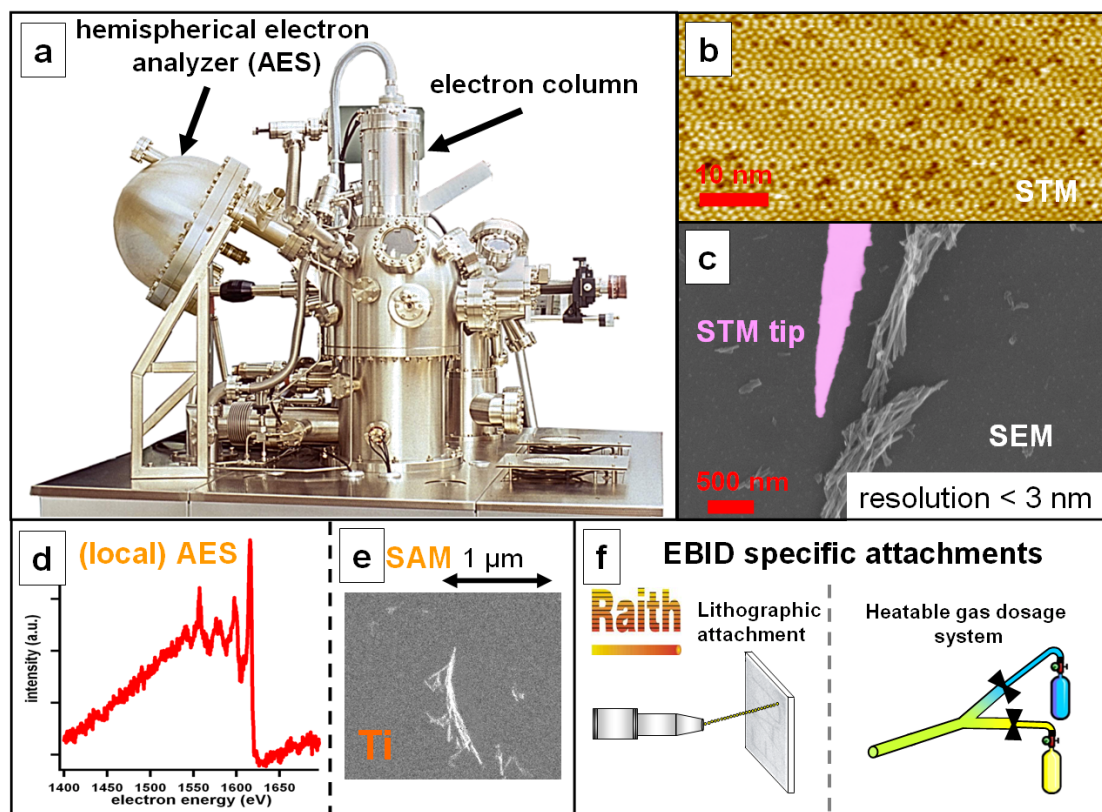


Figure 3.2 Overview of the UHV apparatus, instrumental details and the operation modes: **a)** Photograph of the UHV instrument (Omicron Nanotechnology, Multiscan Lab, base pressure $< 2 \times 10^{-10}$ mbar) utilized for the FEBIP experiments in the work at hand. The UHV compatible electron column (Gemini, Zeiss) and the hemispherical electron analyzer optimized for AES (Omicron nanotechnology) are indicated. **b)** Example for STM operation: atomically resolved 7×7 reconstruction on Si(111). **c)** Example for SEM operation: TiO_x nanotubes on silicon substrate with STM tip (colored purple). **d)** Local Auger electron spectrum (AES) acquired on TiO_x nanotube depicted in **e)**. **e)** Scanning Auger microscopy (SAM) image revealing the distribution of titanium. The bright structure is a bundle of TiO_x nanotubes on a silicon sample. **f)** Illustration of EBID specific attachments, e.g., on the right side the self-constructed heatable gas handling system enabling the simultaneous dosage of two gases

The spatial distribution of the corresponding electrons can be illustrated by the electron interaction cone indicated in orange in Figure 3.1 (compare also Figure 3.5 and the related discussion in Chapter 3.1). Point ii) concerns the vision that using a certain precursor molecule (e.g., organometallic compound) a pure or at least very clean deposit can be generated (e.g., a pure metal from an organometallic precursor). With this approach numerous compounds were utilized in the past to target the fabrication of metallic deposits, containing Fe [137-140], W [20, 25, 28, 141-143], Co [29, 30], Cr [28, 144], Pt [27, 33, 145-147] and Au [27, 33, 145, 148]. A common drawback of EBID is the unintended deposition of precursor fragments [28] or coadsorbed molecules from the residual gas [149] [P12]. A darkening of electron irradiated areas is known since the advent of electron microscopy and can be ascribed to the dissociation of carbon containing residual gases in the vacuum chamber, resulting in a carbon layer appearing darker than the clean surface [150]. This blackening obviously reduces the image quality. Consistent with these observations, it could be shown that with improved vacuum also the image quality could be improved due to less deposited material, and thus minimized darkening in the micrographs [127, 150, 151].

In this Habilitation thesis “surface science type“ EBID experiments were conducted in UHV to reduce the discussed contaminations from the residual gas, but also to guarantee well defined experimental conditions [P12-P16]. Figure 3.2 illustrates the main features of the employed experimental setup. We used an Omicron Nanotechnology Multiscanlab UHV system with a base pressure in the low 10^{-10} mbar regime, which allows to minimize contaminations from the residual gas and to prepare a contamination-free surface. The instrument was financed via a so called HBFNG grant, after evaluation by the Deutsche Forschungsgemeinschaft (DFG); it was delivered in June 2005. The central part of the instrument is an UHV-compatible SEM column, which produces an electron-beam with a diameter of < 3 nm. A hemispherical electron analyzer enables local Auger electron spectroscopy (AES) and scanning Auger microscopy (SAM) with an ultimate resolution better than 10 nm. EBID specific attachments had to be made. The two most important were a self constructed gas handling system for the precursor molecules and lithographic attachments (commercial: Raith, elphy Quantum, and different homemade solutions) to control the electron-beam position on the surface. The whole setup was operable for EBID experiments within the first months of 2006. The EBID process is very complex and relies on manifold parameters. To allow for direct comparison some parameters in the work at hand were kept constant like: 15 kV primary electron beam energy and 400 pA beam current (beam diameter ~ 3 nm) for imaging and EBID, the precursor flow was adjusted to a background pressure of 3×10^{-7} mbar, Auger

spectroscopy (AES) and scanning Auger microscopy (SAM) were performed with 15 kV and ~ 3 nA electron beam, for further details on the experiments please refer to [P13-P16].

In Figure 3.3 the basic ingredients of the experiments conducted so far are depicted. Different precursor molecules were tested. However, in the vast majority of experiments either $\text{Fe}(\text{CO})_5$ or TTIP were dosed as precursors for the fabrication of clean iron or titaniumoxide deposits, respectively. An important aspect was to investigate the influence of the surface. Up to that point the role of the substrate in EBID was mainly considered in respect to the corresponding electron scattering properties of the material [21, 22]. Besides the 300 nm SiO_x on Si all other surfaces were prepared on single crystal samples. Typical surface science methods, like ion sputtering and thermal annealing were applied to prepare the substrates. With AES and low energy electron diffraction (LEED) the cleanliness and the long range atomic order were characterized. In this way well defined and reproducible starting conditions for the EBID process concerning the surface quality could be assured. Also purification procedures for the precursor gases had to be established. The characterization of the precursor quality was done via quadrupole mass spectrometry (QMS).

The discussion of the main results is organized in three subchapters. The presentation of peculiar EBID results, mainly for the system $\text{Fe}(\text{CO})_5$ on Si(001), is followed by the report of different post treatment procedures.

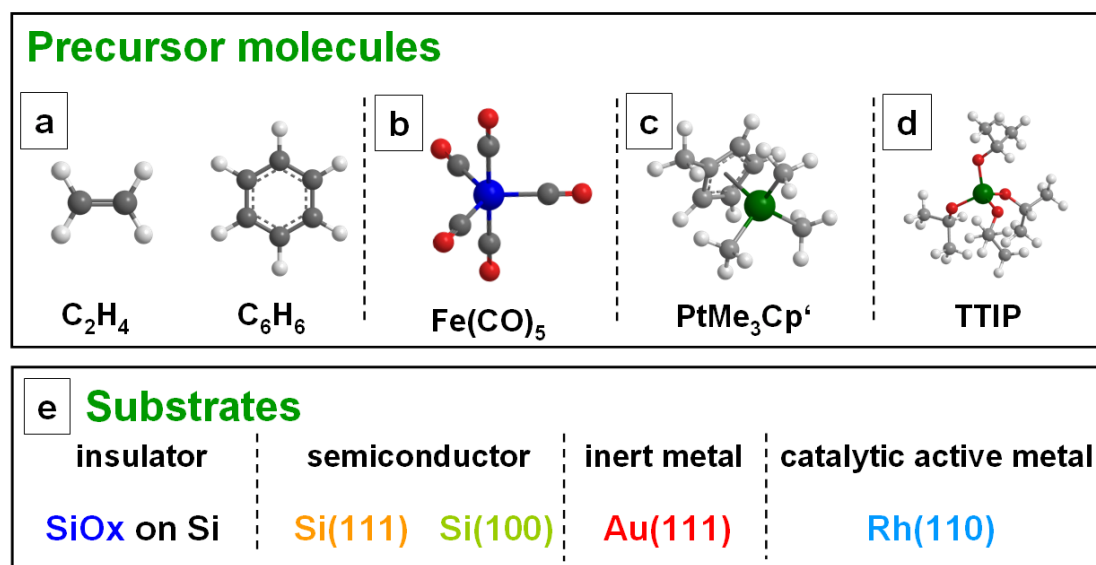


Figure 3.3 Ingredients of the FEBIP experiments in the work at hand. Precursor molecules and targeted deposit materials: **a)** Ethene and benzene; targeted material: carbon. **b)** Ironpentacarbonyl ($\text{Fe}(\text{CO})_5$); targeted material: iron. **c)** Trimethyl-methylcyclopentadienyl-platinum ($\text{PtMe}_3\text{Cp}'$); targeted material: platinum. **d)** Titanium tetrakis(isopropoxy) (TTIP); targeted material: TiO_2 . **e)** Investigated surfaces as substrates in the EBID experiments.

The third subchapter is devoted to the occurrence of catalytic effects already at room temperature. A particularly novel aspect is the electron beam induced local activation of SiO_x surfaces, such that $\text{Fe}(\text{CO})_5$ is selectively decomposed at the pre-irradiated positions. For the latter process the label EBID does not account anymore, therefore the more general term focused electron beam induced processing (FEBIP) is used.

3.1 Results following the “classical” EBID protocol in UHV

In Figure 3.4 a selection of nanostructures written with lithographic control in the EBID approach are depicted. The substrate was Si(111) and different precursor molecules were applied, as indicated in Figure 3.4. In all cases shown in the corresponding figures the main features of the seal structure (compare Fig. 3.4 (d)) could be reproduced and are distinguishable. The contrast of the EBID deposits appear to be different in Figure 3.4 c compared to a and b.

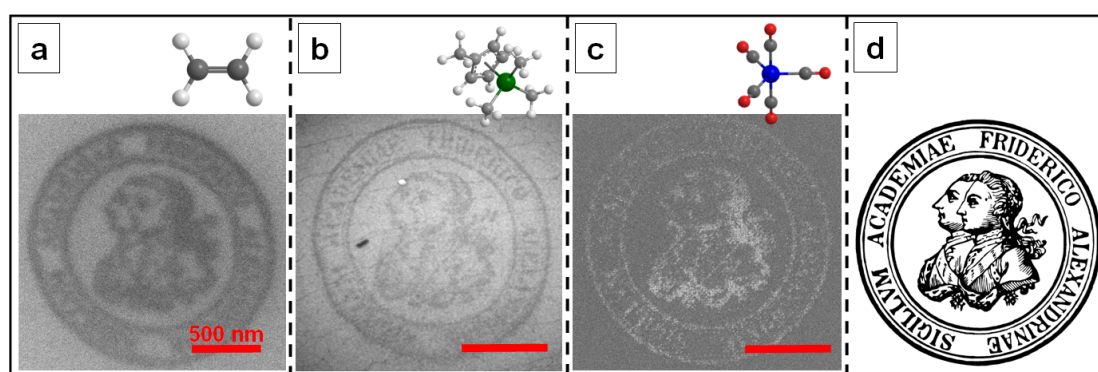


Figure 3.4 Complex template realized on nanometer scale via EBID: SEM images of EBID structures generated with **a)** ethane on Si(111), **b)** trimethyl-methylcyclopentadienyl-platinum on Si(111) and **c)** iron pentacarbonyl on Si(001) template for all deposit was the seal structure shown in **d)**.

Apparently the fabricated structure from $\text{Fe}(\text{CO})_5$ appears brighter than the substrate and in addition the overall appearance of the deposit is rather discontinuous; these observations will be discussed in detail below in context with Figure 3.6. For the continuous structure in Figure 3.4 b the narrowest lines have a diameter below 20 nm, which appears to be the lower limit achievable with our experimental setup and the applied parameters. The main reason is the already mentioned effective broadening of the electron beam due to scattering in the bulk of the sample. In Figure 3.5 this effect is illustrated for a EBID line written with the precursor TTIP on a Au(111) surface.

Apparently the width of the line increases with increasing electron dose. The variation of the electron dose was realized via longer exposure times within one experimental run, i.e., without changing the settings of the SEM. Therefore the diameter of the electron beam can be regarded as constant and thus ruled out as a source of the observed widening. In Figure 3.5 e a simulation of backscattered electrons (BSE) in Ag(111) for the given experimental conditions (15 kV primary beam energy) is depicted. The shape (side view) formed by the BSEs is commonly denoted as BSE cone. Trajectories marked in red represent BS electrons, which exit the surface and thus potentially dissociate adsorbed molecules. The BSEs might also trigger further secondary electrons in inelastic processes which also account for electron induced deposition. The distribution of BSEs exiting the surface has a narrow maximum at the impact point of the electron beam. Assuming a certain amount of electrons needed to fabricate a deposit visible in SEM the widening of the line simply reflects the statistical spatial distribution of the BSEs. One successful strategy to reduce related effects is to use ultrathin substrates and thus to effectively minimize the electron interaction volume leading to a smaller BSE exit area. With this approach van Dorp et al. were able to fabricate EBID deposits smaller than 1 and 3 nm with a TEM and a SEM, respectively [25, 26]. The contrast in the SEM images in Figure 3.5, i.e., the brighter appearance of the substrate can conclusively be explained by the higher atomic number of gold in comparison to titanium, carbon and oxygen as the ingredients of the TTIP precursor (higher atomic number yields more secondary electrons and thus appears brighter in SEM [152, 153]).

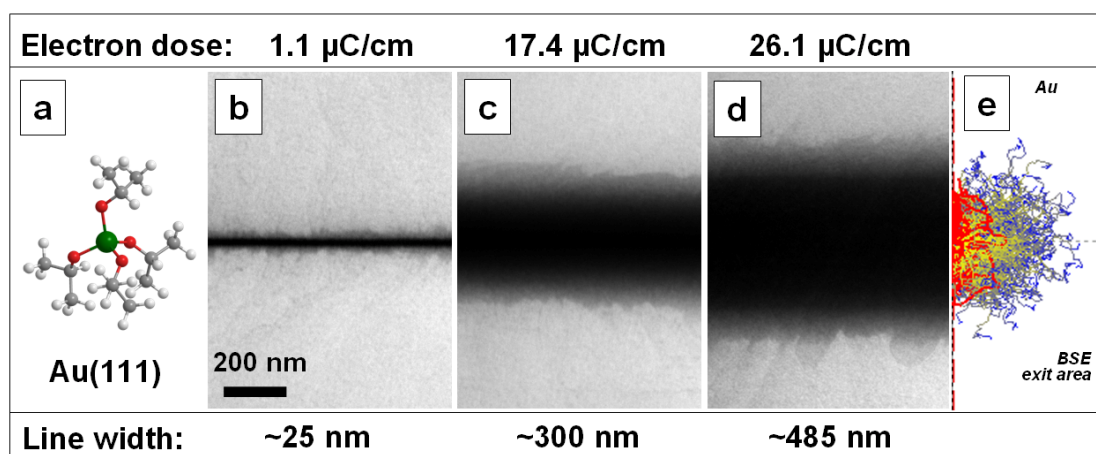


Figure 3.5 Illustration of proximity effects in EBID: **a)** Stick and ball model of the TTIP precursor. **b)-d)** SEM micrographs of lines fabricated with EBID of TTIP on Au(111). **e)** Simulation of the back scattered “electron cone” with Casino V 2.42 [154].

The selected results discussed so far, are in good agreement with the EBID literature. However, EBID with the precursor $\text{Fe}(\text{CO})_5$ on $\text{Si}(001)$ in UHV yielded relevant and novel results as reported in detail in [P13]. In the following a short summary of the most important findings of the latter work will be given. The deposits from $\text{Fe}(\text{CO})_5$ fabricated on $\text{Si}(001)$ at room temperature appear as discontinuous structures consisting of individual dots with a size significantly smaller than 10 nm as depicted in Figure 3.6 a. For the shown dot array an increase of the electron dose will not lead to a broadening of the structures as observed in Figure 3.5, but to more dots, i.e., a higher density of dots. This can be observed in the SEM micrograph in Figure 3.6 c in which a higher dose led to the generation of an area completely packed with dots, such that the substrate is not visible anymore. AE spectroscopy on this field and on the area aside (not irradiated by electrons) yielded the spectra shown in Figure 3.6 d. The iron content of these dots was determined to be >95% based on the AES data. Before the onset of the growth of the dot structures the existence of a continuous prerequisite layer with reduced purity was found. A possible explanation for the formation of the clusters is a high tensile stress relative to the initial layer (probably due to lattice mismatch), which leads to a preference for the formation of small clusters due to an overall energy minimization, with some analogy to the Stranski-Krastanov growth mode [155]. This hypothesis was confirmed by experiments performed at 200 K in which the EBID structures are continuous as shown in Figure 3.6 b, due to the reduced mobility of the involved species. With the findings in [P12] summarized above two main challenges in EBID are successfully addressed, namely the generation of structures smaller than the “classical” limit given by the electron scattering properties of the substrate and the usually rather poor cleanliness of the EBID deposits.

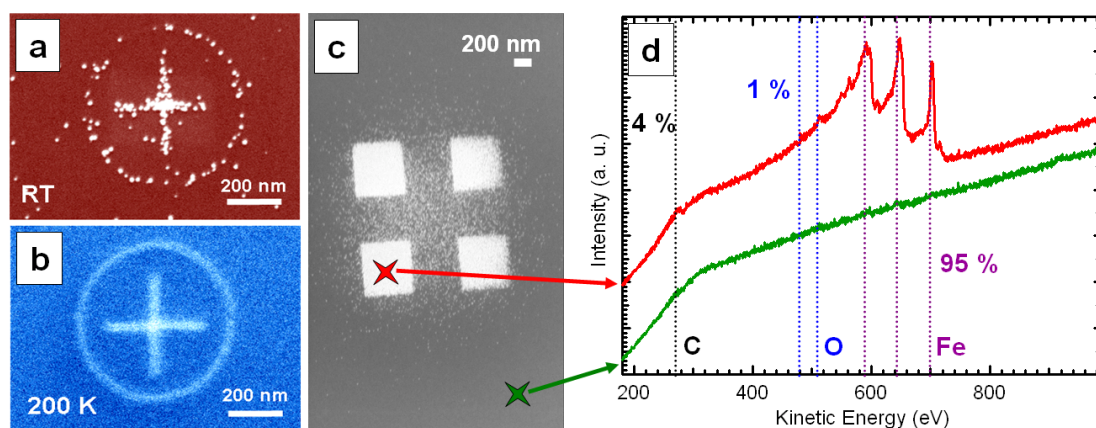


Figure 3.6 Results for EBID in the system $\text{Fe}(\text{CO})_5$ on $\text{Si}(001)$. **a), b)** SEM micrographs of EBID structures (circle and cross) fabricated at the indicated temperatures. Both images were acquired at room temperature. **c)** SEM image of four square area deposits. **d)** AES spectra acquired at the positions indicated in **c)**. The Figure is adapted from [13]

In addition the approach represents a new route towards the lithographic fabrication of (a) ultra clean nanostructures of arbitrary shape and (b) pure metallic nanodots at defined positions with a size below 10 nm, whose density can be controlled from individual dots to densely packed dot fields with a narrow size distribution. It is important to note that the results of the EBID process with $\text{Fe}(\text{CO})_5$ on $\text{Si}(001)$ described above depends on the cleanliness of the ingredients, namely a well defined $\text{Si}(001)$ surface and a purified precursor gas. Therefore, it can be concluded that at least in this case UHV is not only mandatory to reduce the deposition of molecules from the residual gas but also to maintain a well defined surface condition.

3.2 Post treatment procedures

In this subchapter the effect of different post treatment procedures on EBID structures is discussed. Figure 3.7 illustrates how ion sputtering can be employed to reduce the size of EBID deposits. The micrographs in the first row in Figure 3.7 demonstrates the reduction of the width of a particular line deposit from TTIP on $\text{Au}(111)$. The sputtering series also reveals the topography of the deposit. After the first sputtering for 60 minutes the width is reduced from 630 to 220 nm, i.e., by 410 nm.

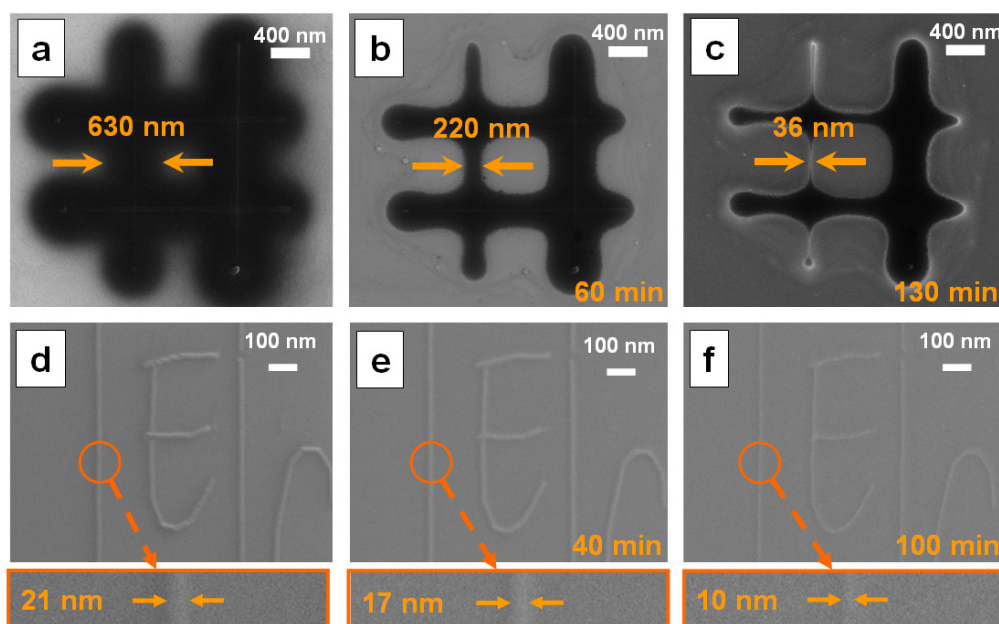


Figure 3.7 Effect of Ar^+ ion sputtering on the shape of EBID deposits: **a)-c)** TTIP/ $\text{Au}(111)$ and **d)-e)** TTIP/ $\text{Si}(001)$. Measured line width and applied total sputter times are indicated in the SEM micrographs. Sputtering was performed with Ar^+ ions with an acceleration voltage of 1 kV and an argon background pressure of 4×10^{-10} mbar.

Even though the second sputtering was applied for additional 70 minutes the line is just narrowed by 184 nm ,i.e., to 36 nm. This evidences that during EBID more material is deposited close to the impact point of the electron beam as already discussed above in the context of Figure 3.5. This finding can be exploited to reduce the lateral size and thus the broadening of EBID deposits due to proximity effects by sputtering. In Figure 3.7 d-e an example is given where the line width of a corresponding EBID deposit (TTIP/Si(001)) is reduced by sputtering below the size directly achievable via EBID with our experimental setup (compare Figure 3.4 b).

The main aspect of the post treatment by sputtering is apparently the size reduction discussed above. In [P16] a post treatment procedure is explored, which transforms the originally amorphous EBID deposits from TTIP on Si(001) into pure TiO_x nanocrystals. In Figure 3.8 the main findings of the study are illustrated. The two crossing lines in Figure 3.8 a represent the starting point of the study, namely an EBID structure consisting of titanium, oxygen but also a significant amount of carbon as contamination (estimated by local AES). The application of TTIP for the current EBID project was initially triggered by metal organic chemical vapor deposition (MOCVD) studies, where the same precursor was used to produce anatase TiO_2 nanoparticles in a flow reactor system [156, 157]. In those studies Berger et al. [156] and Elser et al. [157] purified the also initially carbon contaminated particles by heating the material in an oxygen atmosphere.

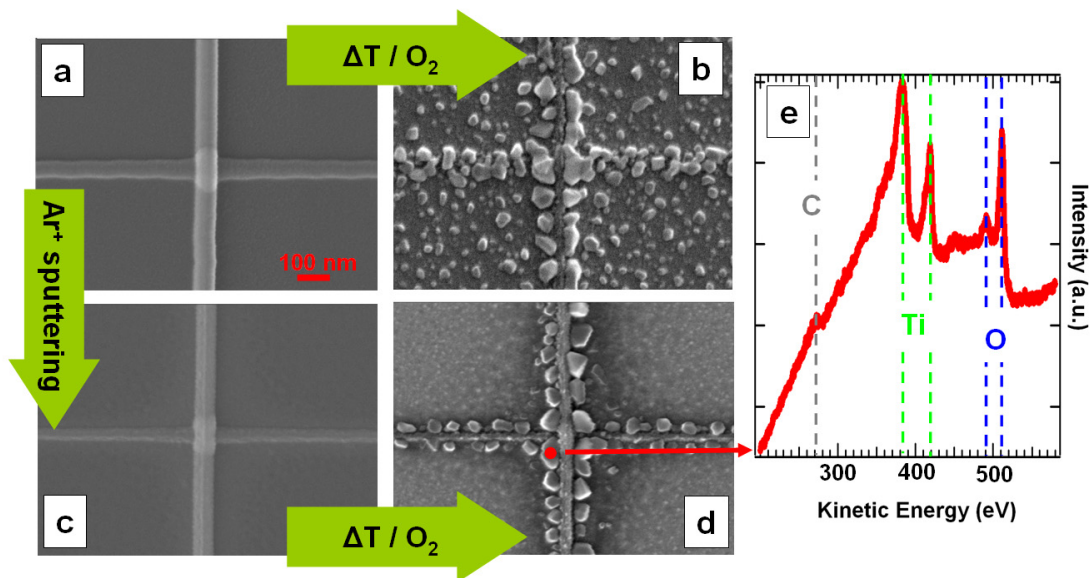


Figure 3.8 Morphology change and purification - post treatment of TTIP EBID deposits on Si(001): **a)** SEM micrograph of as-formed EBID deposit. **b)-d)** EBID structure after indicated post treatments (see text or [P16] for further details). **e)** AES spectrum acquired at position marked in **d)** evidencing the transformation of the previously carbon contaminated deposit to clean TiO_x . The Figure is partially adapted from [16].

But also in EBID the dosage of reactive gases like oxygen during or after the deposition process is known to improve the cleanliness of metal containing deposits [158-160]. The idea behind this cleaning procedure is to oxidize carbon to volatile carbon monoxide (CO) or carbon dioxide (CO₂) and thereby to remove it from the fabricated structures. In addition, heating the sample activates the migration of all components of the EBID deposits, e.g., the migration of carbon to the surface, where it can react with oxygen. The SEM micrograph in Figure 3.8 b evidences the transformation of the initially continuous line deposits into distinct particles. Even though the particles are larger and more dense at the previous positions of the EBID structure, also the unintended generation of scattered particles away from the original line is apparent. This can be traced back to significant deposits in the vicinity of the impact point of the electron beam due to proximity effects. At this point it should be noted that in the specific system, i.e., TTIP on Si(001) the contrast of deposited material and the substrate is very weak, thus local AES data was acquired, which verified the deposition of Ti, O and C in the proximity of the positions directly irradiated by the electron beam. To reduce the amount of deposited material caused by proximity effects the surface was moderately sputtered before the heating/oxygen dosage step. The corresponding micrograph after the ion bombardment is depicted in Figure 3.8 c. Again a transformation of the line structures after heating in oxygen atmosphere is obvious from the SEM image in Figure 3.8 d. Now the small particles are observed exclusively at the positions of the original EBID lines. A special technique developed during the course of the current EBID project, allows to track the position of a single particle during acquisition of a local AES spectrum. A corresponding data set is shown in Figure 3.8 e. The AES spectrum is dominated by titanium and oxygen peaks with a small shoulder assigned to carbon. Based on the shape and local spectroscopic information it is concluded that the particles are indeed pure TiO_x nanocrystals. Consequently the described two-step post-treatment procedure after EBID presents a new pathway for the fabrication of clean, localized nanostructures.

3.3 Catalytic effects

A finding with particular relevance in respect to the controlled growth of pure metallic nanostructures is the observation of catalytic decomposition of Fe(CO)₅ at different surface sites already at room temperature. A sketch of the corresponding localized catalytic processes is depicted in Figure 3.9. The first example to be discussed is the catalytic decomposition of Fe(CO)₅ on clean Rh(110), which is

illustrated in Figure 3.9 a-c and described in detail in [P14]. It was found that the spatial selectivity of the EBID process depends strongly on the actual preparation state of the Rh(110) sample, i.e., for a clean and well defined surface the whole surface is covered with iron. This can be conclusively explained by the catalytic decomposition of $\text{Fe}(\text{CO})_5$ upon adsorption. While CO desorbs, Fe remains as a pure deposit.

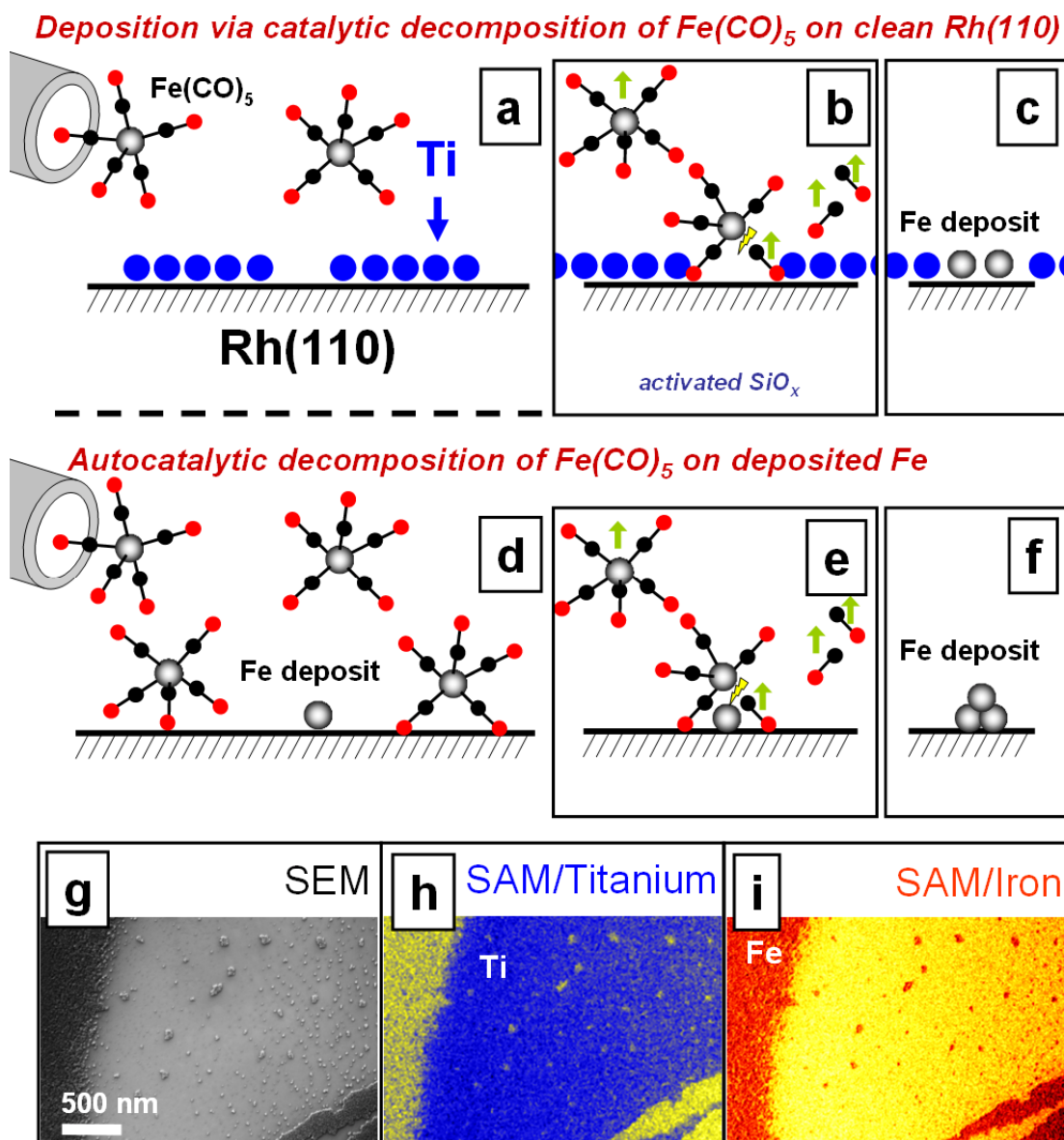


Figure 3.9 Catalytic effects in EBID with $\text{Fe}(\text{CO})_5$ on Rh(111): Sketches of two different decomposition routes of $\text{Fe}(\text{CO})_5$. **a-c)** Selective decomposition of $\text{Fe}(\text{CO})_5$ on clean Rh(110) areas, no deposition on Ti precovered Rh surface. **d-f)** Autocatalytic decomposition on already deposited Fe: (d) $\text{Fe}(\text{CO})_5$ dosage onto surface already covered with predeposited Fe. (e) Autocatalytic decomposition of $\text{Fe}(\text{CO})_5$ on predeposited Fe. (f) Enlarged Fe deposit. **(g-i)** SEM and scanning Auger microscopy (SAM) images of iron deposits on Rh(110) surface partially covered with titanium. The SAM data reveals the distribution of the material in agreement with **a-c)**.

In the following the deposition of Fe continues on the iron deposits via autocatalytic decomposition as sketched in Figure 3.9 d-f. The latter effect was previously reported for $\text{Fe}(\text{CO})_5$ at elevated temperatures [151, 161], similar to the catalytic activity of the Rh(110) surface, which was also extensively studied at elevated temperatures, e.g., for water production from molecular hydrogen and oxygen or the reduction of NO [162-167]. Therefore, it has to be emphasized that the catalytic processes reported here are proceeding already at room temperature. As indicated above the whole process relies on the quality of the surface, i.e., on a sample with reduced quality (slight carbon contaminations, reduced long range order judged by LEED) only a minor amount of Fe is observed on the non irradiated area. On such a sample the EBID process becomes spatially selective again. A way to completely suppress the catalytic activity and thus the Fe growth, is to precover the well defined Rh(110) surface with an ultrathin titanium layer as illustrated by the SEM and the spectromicroscopic scanning Auger microscopy (SAM) images in Figure 3.9 g-i. This finding is sketched in Figure 3 a-c and can be exploited to locally deactivate and therefore pattern the catalytic active surface. An particularly valuable aspect of the autocatalytic growth is the possibility to control the size of the iron deposits by the dosage of the precursor $\text{Fe}(\text{CO})_5$. This concept is demonstrated in Figure 3.10 d for the system $\text{Fe}(\text{CO})_5$ on a 300 nm SiO_x on Si sample [P15]. The upper line was fabricated via EBID and appears darker than the substrate. The bright lines demonstrate the autocatalytic growth of the initial EBID deposit upon prolonged dosage (additional dosage time indicated in the images, please note that the electron doses per line are identical) of the iron precursor without further electron irradiation. The contrast inversion from the upper micrograph to the image below indicates that the initial amount of deposited iron is very low. Therefore one might suspect that the electrons have locally modified the substrate itself, such that it exhibits catalytic activity. This idea is sketched in Figure 3.10 a-c and could be simply verified by irradiation of the surface in UHV, i.e., without $\text{Fe}(\text{CO})_5$. In the next step the precursor was dosed onto the irradiated sample. The result of such a procedure is depicted in Figure 3.10 e: The bright line apparently consists of merged iron nanocrystals, which was confirmed by AES. The proposed mechanism is the electron induced desorption of oxygen leaving reactive vacancies (discussed in detail in [P15]). This idea could be corroborated by similar experiments on an ultra thin ~ 3 nm SiO_x film prepared in situ on a clean Si(001) surface, where charging can practically ruled out as a source for the observed effects. In addition, the realization of the ECCL logo (electron controlled chemical lithography) with the latter method on the ultra thin oxide support is depicted in Figure 3.10 f. Besides the well defined continuous iron lines similar to the ones observed on the 300 nm thick SiO_x support, scattered crystals are observed on the whole surface.

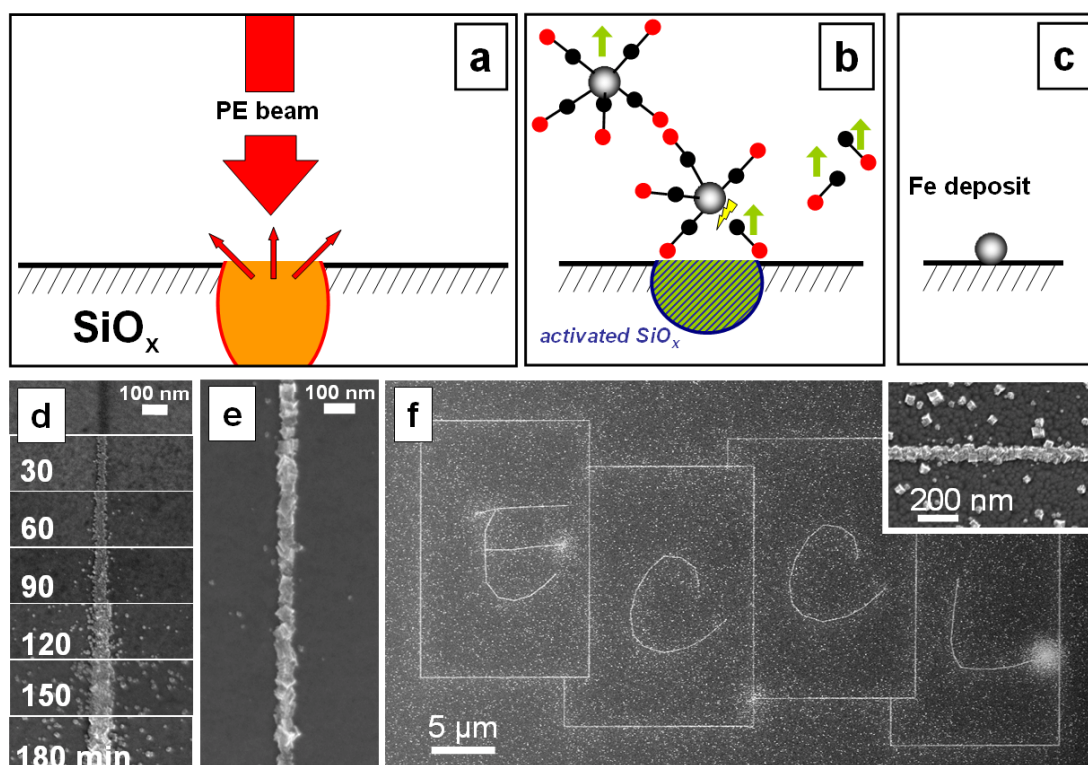


Figure 3.10 Electrons as invisible ink: **a)-c)** Sketch of the electron induced activation of a SiO_x surface **a)**, such that $\text{Fe}(\text{CO})_5$ is decomposed **b)** resulting in a pure iron deposit **c)**. **d)-f)** SEM images of pure iron nanostructures deposited with different electron based techniques with the precursor $\text{Fe}(\text{CO})_5$ on SiO_x surfaces. **d)** Dark line in upper micrograph was generated by conventional EBID on commercial 300 nm SiO_x on Si. The brighter lines below just differ in the additional precursor dosage time indicated in the images. **e)** Line written by FEBIP on a industrial standard 300 nm SiO_x on Si sample, i.e., by exposing the locally electron irradiated surface to the precursor for an extended period of time (here 4.5 h) at RT. **f)** ECCL logo (electron controlled chemical lithography) realized on an ultra thin SiO_x layer (~ 3 nm thick, prepared in UHV) generated with FEBIP. **Insert:** detail of a horizontal line in ECCL logo. The images in **a)-e)** are adapted from [15].

Obviously the preparation of the 3 nm silicon oxide layer is imperfect in the sense that certain sites (probably oxygen vacancies) are active towards the dissociation of $\text{Fe}(\text{CO})_5$. This finding is particularly interesting as a method to fabricate a large number of iron nanoclusters scattered on a macroscopic sample, which size can be controlled by the precursor dosage.

Overall it was evidenced that a highly focused electron beam is capable of locally modifying the properties of a SiO_x surface, such that $\text{Fe}(\text{CO})_5$ dosed after exposure to the electron beam decomposes first catalytically and then autocatalytically already at room temperature (RT), leaving pure iron deposits. In a more vivid description one might think of the process as a way to write nanostructures with electrons as an “invisible ink”, which is then brought to visibility by a development step, i.e., dosing

the precursor. As a consequence, both size and morphology of the generated clean metallic nanostructures can be controlled by the additional gas dosage. It is envisioned that the described effect might be the frontier to a whole new way to generate functional nanostructures.

3.4 Summary, perspective applications and current project activities

The surface science approach to EBID followed in the thesis at hand yielded various novel findings expanding the nanostructure fabrication toolbox. In particular with the generation of pure iron nanostructures from $\text{Fe}(\text{CO})_5$ on different substrates and with different FEBIP protocols a hitherto existing limitation in HV based EBID could be overcome. Also the observation of catalytic and autocatalytic effects already at RT is a novel aspect. Even though the latter findings were all achieved with the precursor $\text{Fe}(\text{CO})_5$ similar effects are anticipated at least for metalcarbonyls like $\text{Co}_2(\text{CO})_8$, $\text{W}(\text{CO})_6$ and $\text{Ni}(\text{CO})_4$, but also other molecules might behave alike. Explorative results (not shown here) also demonstrate that the iron deposits act as seeds for the growth of nanostructures like carbon nanotubes (cooperation with Prof. Nadeja Popovska, Erlangen) and silicon nanowires (cooperation with Dr. Alois Lugstein, Vienna). The growth of the Si nanowires [168-170] on Fe deposits on SiO_x is particularly remarkable since iron was not known to catalyze the growth of the latter. Up to now mostly gold nanoparticles were used as catalysts for Si-wire growth even at a significantly higher temperature than needed for our iron deposits. Generally much effort was put in realizing the assembly of such nanostructures (e.g., [171, 172]), however EBID has the advantage to control the position of the starting point for the nanowires and thus to address the task to arrange the Si-wires. Other ongoing investigations concern the electrical and magnetic properties of the generated iron structures by the group of Prof. Michael Huth (Frankfurt) with corresponding four point probe [173, 174] and Hall sensor micrometer scaled setups. First explorative results evidenced a metallic electron transport behavior (decreasing conductance with increasing temperature) and an overall very high conductance.

Generally the FEBIP process relies on numerous parameters, like energy of primary electron beam, electron beam current density, partial pressure of precursor gas, sample temperature, dosage of additional reactive gases, presence of residual gases, chemical nature and geometry (e.g., thickness) of the sample, condition of the surface (e.g., roughness), lithographic parameters and scan strategy...etc.. As mentioned in the beginning of the work at hand a set of parameters was kept constant; therefore, also these values can be varied to further optimize the results. As a part of this we aim

towards the exploration of different scan strategies, e.g., to agglomerate a particular electron dose in successive irradiation events (sweeps). Hereby we immediately experienced a serious limitation of the commercial lithographic attachment from Raith. Therefore, we are currently developing a homemade solution based on a self written Lab View program. The package is operable (structures depicted in Figures 3.7 d and 3.10 f were realized with the package) and will be tested with a faster hardware to further push the writing speed for one sweep. Another construction, which was just finished, is a dedicated gas handling UHV chamber, fully equipped with all necessary devices to purify the precursor gases and verify their composition. The chamber is tested and fully operable and will be mounted to the main chamber soon. Besides the possibility to attach more gases to the chamber the device will also enhance the overall experimental throughput since the lengthy purification and verification of the precursors can now be performed in a separate chamber.

4 Summary and Outlook

In this thesis the microscopic and spectromicroscopic investigation and fabrication of nanoscaled systems is reported. In the first part porphyrin derivatives on metallic surfaces were investigated by room temperature scanning tunneling microscopy in ultra high vacuum. The microscopic information allowed to determine fundamental aspects of the adsorption behavior of the molecules. The investigated porphyrins self assembled with the macrocycle parallel to the surface in different arrangements depending on the peripheral substituents, the chemical nature of the surface, the sample preparation and coadsorbed small molecules. The detailed analysis of the STM micrographs revealed some fundamental aspects of the ordering mechanisms; in particular the role of molecule/molecule and molecule/substrate interactions could be identified. The obtained findings point towards different strategies to tailor functional molecular networks on metallic surfaces based on the self assembly of porphyrins or more general tetrapyrrolic species. For example, CoTTBPP on Ag(111) was identified to be a suitable candidate for this bottom-up approach: This molecule forms a well defined herringbone phase, which appears to be very rigid due to the interwoven character of the particular supramolecular arrangement.

STM imaging with submolecular resolution enabled to determine the intramolecular conformation of individual molecules. Generally it was found that porphyrins undergo significant deformation upon adsorption, if their macrocycle is lifted from the surface due to the peripheral substituents. With the adsorption of porphyrins on a Cu(111) surface prestructured with oxygen or nickel islands we successfully explored a strategy to locally anchor and / or functionalize tetrapyrrolic molecules

A large part of the thesis focuses on a novel route to functionalize free base porphyrins and phthalocyanines via surface-mediated in situ metalation with Fe, Co and Ni. Hereby the metalation of the free base tetrapyrrolic species proceeds with a yield close to 100 % upon evaporation of the corresponding metal onto the adsorbed molecules. The metalation is especially advantageous in the case of iron porphyrins since these compounds are difficult to handle under ambient conditions.

The local electronic structure of tetraphenyl porphyrins on Ag(111) was investigated in detail to be able to interpret the appearance of the molecules in STM, which can change drastically upon variation of the bias voltage. For that purpose it was crucial to understand the underlying local density of states. This then allowed to trace back the bias voltage dependent appearance of CoTPP to a direct orbital interaction of the adsorbed molecule with the silver substrate and to accurately identify the different porphyrin species in mixed layers.

The second part of the thesis is devoted to the maskless fabrication of pure nanostructures with arbitrary shape by means of focused electron beam processing. The starting point of the investigations was the technique of electron beam induced deposition, in which a highly focused electron beam from an SEM is used to locally dissociate adsorbed precursor molecules, leaving a deposit of the non volatile fragments. In a more vivid picture one might think of the electron beam as a miniaturized pen and the precursor as ink to write nanostructures. Major challenges of conventional EBID are the rather low metal content of deposits from organometallic precursors fabricated in high vacuum environments and the broadening of the deposits in comparison to the electron beam diameter due to interactions of the primary electrons in the substrate, the so-called proximity effects.

Our distinct approach was to perform EBID in an ultra high vacuum environment, first to reduce the amount of unintended deposits from residual gases and thus to improve the cleanliness and secondly to ensure well defined, reproducible conditions. Indeed, using our surface science approach we succeeded to generate pure metallic (iron) and oxidic (iron oxide and titanium oxide) nanostructures from $\text{Fe}(\text{CO})_5$ and TTIP precursors, respectively. For EBID with $\text{Fe}(\text{CO})_5$ on Si(001) the generation of extremely small iron clusters (4-8 nm) was demonstrated. This size surpassed the usual limit of the process determined by proximity effects and could be conclusively explained by lattice mismatch effects between the deposit and substrate.

For the generation of pure TiO_x nanocrystals a novel preparation procedure, comprising ion sputtering and a thermal treatment in oxygen atmosphere, was explored. Another novel aspect concerns the observation of catalytic effects already at room temperature, e.g., iron structures deposited on SiO_x substrates grow upon prolonged dosage of $\text{Fe}(\text{CO})_5$.

One very interesting result was the observation that SiO_2 can be activated by electron irradiation towards the dissociation of subsequently dosed $\text{Fe}(\text{CO})_5$. This novel approach to locally deposit iron deviates from the original EBID protocol and is better described as focused electron beam induced processing (FEBIP). Going back to the initial vivid description one might think of the electrons as invisible ink, which is then brought to visibility by the dosage of the precursor. Besides the microscopic characterization with SEM the spectromicroscopic methods of local Auger electron spectroscopy and scanning Auger microscopy were applied to determine the chemical composition of the deposited structures.

In addition to the specific outlooks at the end of the two main chapters, it is planned to merge the two projects presented in this thesis. The main idea is to generate templates with the focused electron induced techniques to direct the assembly of porphyrins on

the surface. Two routes appear to be especially promising. The first one is the fabrication of nickel deposits on Cu(111) via EBID from the precursor Ni(CO)₄, since it was found that porphyrins tend to locally anchor or even metalate on Ni islands. The second route is based on the finding that the adsorption of porphyrins correlates to the position of preadsorbed oxygen on Cu(111). Based on this observation we suggest to use the electron beam to locally desorb oxygen and thus to fabricate a pattern, which directs the assembly of the porphyrins. Since the SEM instrument is also equipped with a STM, the corresponding experiments will be conducted in one UHV chamber, i.e., without breaking the vacuum. An evaporator for large organic molecules was constructed and tested in a separate chamber and will be mounted to the SEM / STM instrument soon.

In summary one bottom up (self assembly of porphyrins) and one top down approach (FEBIP) to generate nanostructures were explored in UHV mainly at room temperature. In both projects novel aspects of the fabrication techniques were reported expanding the nanostructuring toolbox. The applied state-of-the-art microscopic and spectromicroscopic techniques allowed to gain detailed information on the morphology, chemical composition and the electronic structure of the investigated systems. Some of the corresponding findings enabled new insights into fundamental aspects of the systems like the changes in the electronic structure of CoTPP upon adsorption on a silver surface or the assembly of ultra small iron dots (4-8 nm) in a surface mediated process in EBID.

5 References

1. A. van Leeuwenhoek, *Opera omnia*. 1715-1721.
2. G. Binnig, H. Rohrer, C. Gerber, and E. Weibel, *Surface Studies by Scanning Tunneling Microscopy*. Physical Review Letters, 1982. **49**(1): p. 57 LP - 61.
3. E.W. Müller, *Das Feldionenmikroskop*. Zeitschrift für Physik, 1951. **131**: p. 136-142.
4. G.E. Moore, *Cramming more components onto integrated circuits*. Electronics, 1965. **38**(8): p. n.a.
5. J.V. Barth, G. Costantini, and K. Kern, *Engineering atomic and molecular nanostructures at surfaces*. Nature, 2005. **437**(7059): p. 671-679.
6. J.V. Barth, *Molecular architectonic on metal surfaces*. Annual Review of Physical Chemistry, 2007. **58**: p. 375-407.
7. S. De Feyter and F.C. De Schryver, *Two-dimensional supramolecular self-assembly probed by scanning tunneling microscopy*. Chemical Society Reviews, 2003. **32**(3): p. 139-150.
8. M. de Wild, S. Berner, H. Suzuki, L. Ramoino, A. Baratoff, and T.A. Jung, *Molecular assembly and self-assembly: Molecular nanoscience for future technologies*. Chimia, 2002. **56**(10): p. 500-505.
9. T.A. Jung, R.R. Schlittler, and J.K. Gimzewski, *Conformational identification of individual adsorbed molecules with the STM*. Nature, 1997. **386**(6626): p. 696-698.
10. X.H. Qiu, G.V. Nazin, and W. Ho, *Vibrationally resolved fluorescence excited with submolecular precision*. Science, 2003. **299**(5606): p. 542-546.
11. W. Auwärter, F. Klappenberger, A. Weber-Bargioni, A. Schiffrin, T. Strunskus, C. Wöll, Y. Penneç, A. Riemann, and J.V. Barth, *Conformational Adaptation and Selective Adatom Capturing of Tetrapyrrolyl-porphyrin Molecules on a Copper (111) Surface*. J. Am. Chem. Soc., 2007. **129**(36): p. 11279-11285.
12. W. Auwärter, A. Weber-Bargioni, A. Riemann, A. Schiffrin, O. Groning, R. Fasel, and J.V. Barth, *Self-assembly and conformation of tetrapyrrolyl-porphyrin molecules on Ag(111)*. Journal of Chemical Physics, 2006. **124**(19).
13. A. Weber-Bargioni, W. Auwärter, F. Klappenberger, J. Reichert, S. Lefrançois, T. Strunskus, C. Woll, A. Schiffrin, Y. Penneç, and J.V. Barth, *Visualizing the frontier orbitals of a conformationally adapted metalloporphyrin*. Chemphyschem, 2008. **9**(1): p. 89-94.
14. L. Scudiero, D.E. Barlow, and K.W. Hipps, *Physical Properties and Metal Ion Specific Scanning Tunneling Microscopy Images of Metal(II) Tetraphenylporphyrins Deposited from Vapor onto Gold (111)*. J. Phys. Chem. B, 2000. **104**(50): p. 11899-11905.
15. L. Scudiero, D.E. Barlow, U. Mazur, and K.W. Hipps, *Scanning Tunneling Microscopy, Orbital-Mediated Tunneling Spectroscopy, and Ultraviolet Photoelectron Spectroscopy of Metal(II) Tetraphenylporphyrins Deposited from Vapor*. J. Am. Chem. Soc., 2001. **123**(17): p. 4073-4080.
16. E. Baciocchi, O. Lanzalunga, A. Lapi, and L. Manduchi, *Kinetic Deuterium Isotope Effect Profiles and Substituent Effects in the Oxidative N-Demethylation of N, N - Dimethylanilines Catalyzed by Tetrakis(pentafluorophenyl)porphyrin Iron(III) Chloride*. J. Am. Chem. Soc., 1998. **120**(23): p. 5783-5787.

17. D. Wöhrle, *Porphyryns, phthalocyanines and related systems in polymer phases*. Journal of Porphyrins and Phthalocyanines, 2000. **4**(4): p. 418-424.
18. D. Mansuy and P. Battioni, *Diversity of reactions catalyzed by heme-thiolate proteins*, in *The Porphyrin Handbook*, K.M. Kadish, K.M. Smith, and R. Guilard, Editors. 2000, Academic Press: San Diego. p. 1-14.
19. K.M. Kadish, *The Porphyrin Handbook*. Chlorophylls and Bilins: Biosynthesis, Synthesis, and Degradation. Vol. Vol. 13. 2003, San Diego.
20. H.W.P. Koops, R. Weiel, D.P. Kern, and T.H. Baum, *High-resolution electron-beam induced deposition*. Journal of Vacuum Science & Technology B: Microelectronics and Nanometer Structures, 1988. **6**(1): p. 477-481.
21. W.F. van Dorp and C.W. Hagen, *A critical literature review of focused electron beam induced deposition*. Journal of Applied Physics, 2008. **104**(8): p. 081301/1-081301/42.
22. I. Utke, P. Hoffman, and J. Melngailis, *Gas-assisted focused electron beam and ion beam processing and fabrication*. Journal of Vacuum Science & Technology B: Microelectronics and Nanometer Structures, 2008. **24**(6): p. 1197-1276.
23. S.J. Randolph, J.D. Fowlkes, and P.D. Rack, *Focused, Nanoscale Electron-Beam-Induced Deposition and Etching*. Critical Reviews in Solid State & Materials Science, 2006. **31**(3): p. 55-89.
24. K. Edinger, H. Becht, J. Bihl, V. Boegli, M. Budach, T. Hofmann, H.W.P. Koops, P. Kuschnerus, J. Oster, P. Spies, and B. Weyrauch, *Electron-beam-based photomask repair*. Journal of Vacuum Science & Technology B: Microelectronics and Nanometer Structures, 2004. **2**(6): p. 2902-2906.
25. W.F. van Dorp, B. van Someren, C.W. Hagen, and P. Kruit, *Approaching the Resolution Limit of Nanometer-Scale Electron Beam-Induced Deposition*. Nano Letters, 2005. **5**(7): p. 1303-1307.
26. L. van Kouwen, A. Botman, and C.W. Hagen, *Focused Electron-Beam-Induced Deposition of 3 nm Dots in a Scanning Electron Microscope*. Nano Letters, 2009. **9**(5): p. 2149-2152.
27. M. Weber, H.W.P. Koops, M. Rudolph, J. Kretz, and G. Schmidt, *New compound quantum dot materials produced by electron-beam induced deposition*. Journal of Vacuum Science & Technology B: Microelectronics and Nanometer Structures, 1995. **13**(3): p. 1364-1368.
28. S. Matsui and K. Mori, *New selective deposition technology by electron-beam induced surface reaction*. Journal of Vacuum Science & Technology B: Microelectronics and Nanometer Structures, 1986. **4**(1): p. 299-304.
29. Y.M. Lau, P.C. Chee, J.T.L. Thong, and V. Ng, *Properties and applications of cobalt-based material produced by electron-beam-induced deposition*. Journal of Vacuum Science & Technology A: Vacuum, Surfaces, and Films, 2002. **20**(4): p. 1295-1302.
30. I. Utke, P. Hoffmann, R. Berger, and L. Scandella, *High-resolution magnetic Co supertips grown by a focused electron beam*. Applied Physics Letters, 2002. **80**(25): p. 4792-4794.
31. Y. Ochiai, J.-i. Fujita, and S. Matsui, *Electron-beam-induced deposition of copper compound with low resistivity*. Journal of Vacuum Science & Technology B: Microelectronics and Nanometer Structures, 1996. **14**(6): p. 3887-3891.
32. F. Cicoira, P. Hoffmann, C.O.A. Olsson, N. Xanthopoulos, H.J. Mathieu, and P. Doppelt, *Auger electron spectroscopy analysis of high metal content micro-structures grown by electron beam induced deposition*. Applied Surface Science, 2005. **242**(1-2): p. 107-113.

33. H.W.P. Koops, C. Schossler, A. Kaya, and M. Weber, *Conductive dots, wires, and supertips for field electron emitters produced by electron-beam induced deposition on samples having increased temperature*. Journal of Vacuum Science & Technology B, 1996. **14**(6): p. 4105-4109.
34. A. Perentes, G. Sinicco, G. Boero, B. Dwir, and P. Hoffmann, *Focused electron beam induced deposition of nickel*. Journal of Vacuum Science & Technology B: Microelectronics and Nanometer Structures, 2007. **25**(6): p. 2228-2232.
35. T. Bret, I. Utke, A. Bachmann, and P. Hoffmann, *In situ control of the focused-electron-beam-induced deposition process*. Applied Physics Letters, 2003. **83**(19): p. 4005-4007.
36. O. Yavas, C. Ochiai, M. Takai, A. Hosono, and S. Okuda, *Maskless fabrication of field-emitter array by focused ion and electron beam*. Applied Physics Letters, 2000. **76**(22): p. 3319-3321.
37. I. Utke, B. Dwir, K. Leifer, F. Cicoira, P. Doppelt, P. Hoffman, and E. Kapon, *Electron beam induced deposition of metallic tips and wires for microelectronics applications*. Applied Physics Letters, 2000. **53**(1-4): p. 261-264.
38. K.L. Lee and M. Hatzakis, *Direct electron-beam patterning for nanolithography*. Journal of Vacuum Science & Technology B: Microelectronics and Nanometer Structures, 1989. **7**(6): p. 1941-1946.
39. A. Perentes, T. Bret, I. Utke, P. Hoffmann, and M. Vaupel, *Real-time reflectometry-controlled focused-electron-beam-induced deposition of transparent materials*. Journal of Vacuum Science & Technology B: Microelectronics and Nanometer Structures, 2006. **24**(2): p. 587-591.
40. I. Mochida, K. Suetsugu, H. Fujitsu, and K. Takeshita, *Enhanced Catalytic Activity of Cobalt Tetraphenylporphyrin on Titanium Dioxide by Evacuation at Elevated Temperatures for Intensifying the Complex-Support Interaction*. Journal of Physical Chemistry, 1983. **87**: p. 1524-1529.
41. S. Berner, S. Biela, G. Ledung, A. Gogoll, J.E. Backvall, C. Puglia, and S. Oscarsson, *Activity boost of a biomimetic oxidation catalyst by immobilization onto a gold surface*. Journal of Catalysis, 2006. **244**(1): p. 86-91.
42. I.O. Benitez, B. Bujoli, L.J. Camus, C.M. Lee, F. Odobel, and D.R. Talham, *Monolayers as models for supported catalysts: Zirconium phosphonate films containing manganese(III) porphyrins*. Journal of the American Chemical Society, 2002. **124**(16): p. 4363-4370.
43. B. Hulsken, R. Van Hameren, J.W. Gerritsen, T. Khoury, P. Thordarson, M.J. Crossley, A.E. Rowan, R.J.M. Nolte, J.A.A.W. Elemans, and S. Speller, *Real-time single-molecule imaging of oxidation catalysis at a liquid-solid interface*. Nature Nanotechnology, 2007. **2**(5): p. 285-289.
44. W.J.R. Santos, A.L. Sousa, R.C.S. Luz, F.S. Damos, L.T. Kubota, A.A. Tanaka, and S.M.C.N. Tanaka, *Amperometric sensor for nitrite using a glassy carbon electrode modified with alternating layers of iron(III) tetra-(N-methyl-4-pyridyl)-porphyrin and cobalt(II) tetrasulfonated phthalocyanine*. Talanta, 2006. **70**(3): p. 588-594.
45. G. Ashkenasy, A. Ivanisevic, R. Cohen, C.E. Felder, D. Cahen, A.B. Ellis, and A. Shanzer, *Assemblies of "hinged" iron-porphyrins as potential oxygen sensors*. Journal of the American Chemical Society, 2000. **122**(6): p. 1116-1122.
46. G. Guillaud, J. Simon, and J.P. Germain, *Metallophthalocyanines: Gas sensors, resistors and field effect transistors*. Coordination Chemistry Reviews, 1998. **178-180**: p. 1433-1484.
47. N.A. Rakow and K.S. Suslick, *A colorimetric sensor array for odour visualization*. Nature, 2000. **406**(6797): p. 710-713.

48. B.R. Takulapalli, G.M. Laws, P.A. Liddell, J. Andreasson, Z. Erno, D. Gust, and T.J. Thornton, *Electrical detection of amine ligation to a metalloporphyrin via a hybrid SOI-MOSFET*. Journal of the American Chemical Society, 2008. **130**(7): p. 2226-2233.
49. H. Imahori and S. Fukuzumi, *Porphyrin- and fullerene-based molecular photovoltaic devices*. Advanced Functional Materials, 2004. **14**(6): p. 525-536.
50. D.S. Hecht, R.J.A. Ramirez, M. Briman, E. Artukovic, K.S. Chichak, J.F. Stoddart, and G. Gruner, *Bioinspired detection of light using a porphyrin-sensitized single-wall nanotube field effect transistor*. Nano Letters, 2006. **6**(9): p. 2031-2036.
51. T. Hasobe, H. Imahori, H. Yamada, T. Sato, K. Ohkubo, and S. Fukuzumi, *Enhancement of light harvesting and photocurrent generation by ITO electrodes modified with meso,meso-linked porphyrin oligomers*. Nano Letters, 2003. **3**(3): p. 409-412.
52. G.V. Nazin, X.H. Qiu, and W. Ho, *Visualization and spectroscopy of a metal-molecule-metal bridge*. Science, 2003. **302**(5642): p. 77-81.
53. X.H. Qiu, G.V. Nazin, and W. Ho, *Mechanisms of Reversible Conformational Transitions in a Single Molecule*. Physical Review Letters, 2004. **93**(19): p. 196806-4.
54. F. Moresco, G. Meyer, K.H. Rieder, H. Ping, H. Tang, and C. Joachim, *TBPP molecules on copper surfaces: a low temperature scanning tunneling microscope investigation*. Surface Science, 2002. **499**(1): p. 94-102.
55. F. Moresco, G. Meyer, K.-H. Rieder, J. Ping, H. Tang, and C. Joachim, *TBPP molecules on copper surfaces: a low temperature scanning tunneling microscope investigation*. Surface Science, 2002. **499**(1): p. 94-102.
56. T. Lukasczyk, K. Flechtner, L.R. Merte, N. Jux, F. Maier, J.M. Gottfried, and H.-P. Steinrück, *Interaction of Cobalt(II) Tetraarylporphyrins with a Ag(111) Surface Studied with Photoelectron Spectroscopy*. J. Phys. Chem. C, 2007. **111**(7): p. 3090-3098.
57. A. Weber-Bargioni, J. Reichert, A.P. Seitsonen, W. Auwärter, A. Schiffrin, and J.V. Barth, *Interaction of Cerium Atoms with Surface-Anchored Porphyrin Molecules*. J. Phys. Chem. C, 2008. **112**(10): p. 3453-3455.
58. H. Spillmann, A. Kiebele, M. Stöhr, T.A. Jung, D. Bonifazi, F.Y. Cheng, and F. Diederich, *A two-dimensional porphyrin-based porous network featuring communicating cavities for the templated complexation of fullerenes*. Advanced Materials, 2006. **18**(3): p. 275-+.
59. M. Stöhr, T. Wagner, M. Gabriel, B. Weyers, and R. Moller, *Binary molecular layers of C-60 and copper phthalocyanine on Au(111): Self-organized nanostructuring*. Advanced Functional Materials, 2001. **11**(3): p. 175-178.
60. S. Yoshimoto, N. Higa, and K. Itaya, *Two-dimensional supramolecular organization of copper octaethylporphyrin and cobalt phthalocyanine on Au(III): Molecular assembly control at an electrochemical interface*. Journal of the American Chemical Society, 2004. **126**(27): p. 8540-8545.
61. A. Kretschmann, M.M. Walz, K. Flechtner, H.P. Steinrück, and J.M. Gottfried, *Tetraphenylporphyrin picks up zinc atoms from a silver surface*. Chem. Commun., 2007(6): p. 568-570.
62. J.M. Gottfried, K. Flechtner, A. Kretschmann, T. Lukasczyk, and H.-P. Steinrück, *Direct Synthesis of a Metalloporphyrin Complex on a Surface*. J. Am. Chem. Soc., 2006. **128**(17): p. 5644-5645.
63. L. Scudiero, D.E. Barlow, and K.W. Hipps, *Scanning tunneling microscopy, orbital-mediated tunneling spectroscopy, and ultraviolet photoelectron spectroscopy of nickel(II) octaethylporphyrin deposited from vapor*. J. Phys. Chem. B, 2002. **106**(5): p. 996-1003.

64. A. Ogunrinde, K.W. Hipps, and L. Scudiero, *A Scanning Tunneling Microscopy Study of Self-Assembled Nickel(II) Octaethylporphyrin Deposited from Solutions on HOPG*. *Langmuir*, 2006. **22**(13): p. 5697-5701.
65. S. Yoshimoto, E. Tsutsumi, Y. Honda, Y. Murata, M. Murata, K. Komatsu, O. Ito, and K. Itaya, *Controlled molecular orientation in an adlayer of a supramolecular assembly consisting of an open-cage C-60 derivative and Zn-II octaethylporphyrin on Au(111)*. *Angewandte Chemie-International Edition*, 2004. **43**(23): p. 3044-3047.
66. S. Yoshimoto, A. Tada, and K. Itaya, *In situ scanning tunneling microscopy study of the effect of iron octaethylporphyrin adlayer on the electrocatalytic reduction of O₂ on Au(111)*. *Journal of Physical Chemistry B*, 2004. **108**(17): p. 5171-5174.
67. Y. Zhang, X. Tao, H.Y. Gao, Z.C. Dong, J.G. Hou, and T. Okamoto, *Modulation of local plasmon mediated emission through molecular manipulation*. *Physical Review B*, 2009. **79**(7).
68. A. Kirakosian, J.-L. Lin, D.Y. Petrovykh, J.N. Crain, and F.J. Himpsel, *Functionalization of silicon step arrays I: Au passivation of stepped Si(111) templates*. *Journal of Applied Physics*, 2001. **90**(7): p. 3286-3290.
69. A.V. Zotov, D.V. Gruznev, O.A. Utas, V.G. Kotlyar, and A.A. Saranin, *Multi-mode growth in Cu/Si(111) system: Magic nanoclustering, layer-by-layer epitaxy and nanowire formation*. *Surface Science*, 2008. **602**(1): p. 391-398.
70. H. Yanagi, H. Mukai, K. Ikuta, T. Shibutani, T. Kamikado, S. Yokoyama, and S. Mashiko, *Molecularly resolved dynamics for two-dimensional nucleation of supramolecular assembly*. *Nano Letters*, 2002. **2**(6): p. 601-604.
71. T. Wölfle, A. Gorling, and W. Hieringer, *Conformational flexibility of metalloporphyrins studied by density-functional calculations*. *Physical Chemistry Chemical Physics*, 2008. **10**(37): p. 5739-5742.
72. J. Brede, M. Linares, S. Kuck, J. Schwobel, A. Scarfato, S.-H. Chang, G. Hoffmann, R. Wiesendanger, R. Lensen, P.H.J. Kouwer, J. Hoogboom, A.E. Rowan, M. Broring, M. Funk, S. Stafstrom, F. Zerbetto, and R. Lazzaroni, *Dynamics of molecular self-ordering in tetraphenyl porphyrin monolayers on metallic substrates*. *Nanotechnology*, 2009. **20**(27): p. 275602.
73. K. Comanici, *Clean porphyrin films on a silver (111) surface: a Scanning Tunneling Microscopy study*, in *PhD*. 2007.
74. F. Buchner, *STM Investigation of Molecular Architectures of Porphinoids on a Ag(111) Surface*. PhD thesis, Erlangen 2010.
75. S. Burley and G. Petsko, *Aromatic-aromatic interaction: a mechanism of protein structure stabilization*. *Science*, 1985. **229**(4708): p. 23-28.
76. R.K.C. Emmanuel A. Meyer, François Diederich, *Interactions with Aromatic Rings in Chemical and Biological Recognition*. *Angewandte Chemie International Edition*, 2003. **42**(11): p. 1210-1250.
77. E.G. Cox, D.W.J. Cruickshank, and J.A.S. Smith, *The Crystal Structure of Benzene at -3° C*. *Proceedings of the Royal Society of London. Series A. Mathematical and Physical Sciences*, 1958. **247**(1248): p. 1-21.
78. R. Laatikainen, J. Ratilainen, R. Sebastian, and H. Santa, *NMR Study of Benzene and Some Other Fundamental Aromatic Systems Using Alignment of Aromatics in Strong Magnetic Field*. *Journal of the American Chemical Society*, 2002. **117**(44): p. 11006-11010.
79. D. Ecija, M. Trelka, C. Urban, P.d. Mendoza, E. Mateo-Marti, C. Rogero, J.A. Martin-Gago, A.M. Echavarren, R. Otero, J.M. Gallego, and R. Miranda, *Molecular Conformation, Organizational Chirality, and Iron Metalation of meso-Tetramesitylporphyrins on Copper(100)*. *J. Phys. Chem. C*, 2008.

80. K.H. Ernst, *Supramolecular surface chirality*, in *Supramolecular Chirality*. 2006, SPRINGER-VERLAG BERLIN: Berlin. p. 209-252.
81. K.H. Ernst, *Aspects of Molecular Chirality at Metal Surfaces*. Zeitschrift Fur Physikalische Chemie-International Journal of Research in Physical Chemistry & Chemical Physics, 2009. **223**(1-2): p. 37-51.
82. R. Fasel, M. Parschau, and K.-H. Ernst, *Amplification of chirality in two-dimensional enantiomorphous lattices*. 2006. **439**(7075): p. 449-452.
83. E. Zillner, *Dynamics and Ordering Aspects of Porphyrins on a Plain and Prestructured Copper (111) Surface: A Scanning Tunneling Microscopy Study*. Master thesis, Erlangen, 2009.
84. M. Eichberger, M. Marschall, J. Reichert, A. Weber-Bargioni, W. Auwärter, R.L.C. Wang, H.J. Kreuzer, Y. Pennec, A. Schiffrin, and J.V. Barth, *Dimerization Boosts One-Dimensional Mobility of Conformationally Adapted Porphyrins on a Hexagonal Surface Atomic Lattice*. Nano Letters, 2008. **8**(12): p. 4608-4613.
85. J.V. Barth, *Transport of adsorbates at metal surfaces: From thermal migration to hot precursors*. Surface Science Reports, 2000. **40**(3-5): p. 75-149.
86. C. Loppacher, M. Guggisberg, O. Pfeiffer, E. Meyer, M. Bammerlin, R. Luthi, R. Schlittler, J.K. Gimzewski, H. Tang, and C. Joachim, *Direct determination of the energy required to operate a single molecule switch*. Physical Review Letters, 2003. **90**(6).
87. F. Moresco, G. Meyer, K.H. Rieder, H. Tang, A. Gourdon, and C. Joachim, *Conformational changes of single molecules induced by scanning tunneling microscopy manipulation: A route to molecular switching*. Physical Review Letters, 2001. **86**(4): p. 672-675.
88. F. Moresco, G. Meyer, K.H. Rieder, H. Tang, A. Gourdon, and C. Joachim, *Recording intramolecular mechanics during the manipulation of a large molecule*. Physical Review Letters, 2001. **8708**(8).
89. T. Kamikado, T. Sekiguchi, S. Yokoyama, Y. Wakayama, and S. Mashiko, *Control of single supramolecular chain of porphyrin on a copper surface*. Thin Solid Films, 2006. **499**(1-2): p. 329-332.
90. W. Auwärter, A. Weber-Bargioni, S. Brink, A. Riemann, A. Schiffrin, M. Ruben, and J.V. Barth, *Controlled metalation of self-assembled porphyrin nanoarrays in two dimensions*. Chemphyschem, 2007. **8**(2): p. 250-254.
91. F. Vollnhals, *Octaethylporphyrins on a Silver (111) Surface: A Scanning Tunneling Microscopy Study*. Master thesis, Erlangen 2009.
92. H. Brune, M. Giovannini, K. Bromann, and K. Kern, *Self-organized growth of nanostructure arrays on strain-relief patterns*. Nature, 1998. **394**(6692): p. 451-453.
93. K. Morgenstern, J. Kibsgaard, J.V. Lauritsen, E. Laegsgaard, and F. Besenbacher, *Cobalt growth on two related close-packed noble metal surfaces*. Surface Science, 2007. **601**(9): p. 1967-1972.
94. H. Brune, *Microscopic view of epitaxial metal growth: nucleation and aggregation*. Surface Science Reports, 1998. **31**(4-6): p. 125-229.
95. F. Besenbacher, *Scanning tunnelling microscopy studies of metal surfaces*. Reports on Progress in Physics, 1996. **59**(12): p. 1737-1802.
96. C. Wagner, R. Franke, and T. Fritz, *Evaluation of I(V) curves in scanning tunneling spectroscopy of organic nanolayers*. Physical Review B, 2007. **75**(23): p. 235432.
97. J.A. Stroscio and W.J. Kaiser, eds. *Scanning Tunneling Microscopy*. 1993, Academic Press, New York.

98. M. Ruben, J.-M. Lehn, and P. Muller, *Addressing metal centres in supramolecular assemblies*. Chemical Society Reviews, 2006. **35**(11): p. 1056-1067.
99. K. Flechtner, A. Kretschmann, H.-P. Steinrück, and J.M. Gottfried, *NO-Induced Reversible Switching of the Electronic Interaction between a Porphyrin-Coordinated Cobalt Ion and a Silver Surface*. J. Am. Chem. Soc., 2007. **129**(40): p. 12110-+.
100. X. Lu, K.W. Hipps, X.D. Wang, and U. Mazur, *Scanning tunneling microscopy of metal phthalocyanines: d(7) and d(9) cases*. Journal of the American Chemical Society, 1996. **118**(30): p. 7197-7202.
101. X. Lu and K.W. Hipps, *Scanning tunneling microscopy of metal phthalocyanines: d(6) and d(8) cases*. Journal of Physical Chemistry B, 1997. **101**(27): p. 5391-5396.
102. G. Kresse and J. Furthmuller, *Efficient iterative schemes for ab initio total-energy calculations using a plane-wave basis set*. Physical Review B, 1996. **54**(16): p. 11169-11186.
103. G. Kresse and J. Furthmuller, *Efficiency of ab-initio total energy calculations for metals and semiconductors using a plane-wave basis set*. Computational Materials Science, 1996. **6**(1): p. 15-50.
104. G. Kresse and J. Hafner, *Ab initio molecular dynamics for open-shell transition metals*. Physical Review B, 1993. **48**(17): p. 13115 LP - 13118.
105. J. Tersoff and D.R. Hamann, *Theory and Application for the Scanning Tunneling Microscope*. Physical Review Letters, 1983. **50**(25): p. 1998 LP - 2001.
106. J. Tersoff and D.R. Hamann, *Theory of the scanning tunneling microscope*. Physical Review B, 1985. **31**(2): p. 805 LP - 813.
107. M. Lackinger, T. Muller, T.G. Gopakumar, F. Muller, M. Hietschold, and G.W. Flynn, *Tunneling Voltage Polarity Dependent Submolecular Contrast of Naphthalocyanine on Graphite. A STM Study of Close-Packed Monolayers under Ultrahigh-Vacuum Conditions*. J. Phys. Chem. B, 2004. **108**(7): p. 2279-2284.
108. L.A. Zotti, G. Teobaldi, W.A. Hofer, W. Auwarter, A. Weber-Bargioni, and J.V. Barth, *Ab-initio calculations and STM observations on tetrapyrrolyl and Fe(II)-tetrapyrrolyl-porphyrin molecules on Ag(1 1 1)*. Surface Science, 2007. **601**(12): p. 2409-2414.
109. K.W. Hipps, L. Scudiero, D.E. Barlow, and M.P. Cooke, *A self-organized 2-dimensional bifunctional structure formed by supramolecular design*. Journal of the American Chemical Society, 2002. **124**(10): p. 2126-2127.
110. L. Scudiero, K.W. Hipps, and D.E. Barlow, *A Self-Organized Two-Dimensional Bimolecular Structure*. J. Phys. Chem. B, 2003. **107**(13): p. 2903-2909.
111. D. Bonifazi, H. Spillmann, A. Kiebele, M. de Wild, P. Seiler, F.Y. Cheng, H.J. Guntherodt, T. Jung, and F. Diederich, *Supramolecular patterned surfaces driven by cooperative assembly of C-60 and porphyrins on metal substrates*. Angewandte Chemie-International Edition, 2004. **43**(36): p. 4759-4763.
112. M. de Wild, S. Berner, H. Suzuki, H. Yanagi, D. Schlettwein, S. Ivan, A. Baratoff, H.J. Guntherodt, and T.A. Jung, *A novel route to molecular self-assembly: Self-intermixed monolayer phases*. Chemphyschem, 2002. **3**(10): p. 881-885.
113. Z.Y. Yang, S.B. Lei, L.H. Gan, L.J. Wan, C. Wang, and C.L. Bai, *The effect of polarity on coadsorbed molecular nanostructures of substituted phthalocyanine and thiol molecules*. Chemphyschem, 2005. **6**(1): p. 65-70.
114. D.X. Wu, K. Deng, M. He, Q.D. Zeng, and C. Wang, *Coadsorption-induced reconstruction of supramolecular assembly characteristics*. Chemphyschem, 2007. **8**(10): p. 1519-1523.
115. V. Schwald, *Der Einfluss von NO/CO auf Porphyrin-Monolagen*. Zulassungsarbeit, Erlangen, 2007.

116. A. Turchanin, A. Beyer, C.T. Nottbohm, X.H. Zhang, R. Stosch, A. Sologubenko, J. Mayer, P. Hinze, T. Weimann, and A. Golzhauser, *One Nanometer Thin Carbon Nanosheets with Tunable Conductivity and Stiffness*. *Advanced Materials*, 2009. **21**(12): p. 1233.
117. A. Turchanin, D. Kafer, M. El-Desawy, C. Woll, G. Witte, and A. Golzhauser, *Molecular Mechanisms of Electron-Induced Cross-Linking in Aromatic SAMs*. *Langmuir*, 2009. **25**(13): p. 7342-7352.
118. A.C. Papageorgiou, C.L. Pang, Q. Chen, and G. Thornton, *Low-dimensional, reduced phases of ultrathin TiO₂*. *Acs Nano*, 2007. **1**(5): p. 409-414.
119. T. Hamann, E. Bohler, and P. Swiderek, *Low-Energy-Electron-Induced Hydroamination of an Alkene*. *Angewandte Chemie-International Edition*, 2009. **48**(25): p. 4643-4645.
120. C.R. Arumainayagam, H.L. Lee, R.B. Nelson, D.R. Haines, and R.P. Gunawardane, *Low-energy electron-induced reactions in condensed matter*. *Surface Science Reports*, 2010. **65**(1): p. 1-44.
121. B.A. Joyce and J.H. Neave, *Electron beam-adsorbate interactions on silicon surfaces*. *Surface Science*, 1973. **34**(2): p. 401-419.
122. C. Klauber, M.D. Alvey, and J.T. Yates Jr., *NH₃ adsorption on Ni(110) and the production of the NH₂ species by electron irradiation*. *Surface Science*, 1985. **154**(1): p. 139-167.
123. R.D. Ramsier and J.T. Yates, *Electron-stimulated desorption: Principles and applications*. *Surface Science Reports*, 1991. **12**(6-8): p. 246-378.
124. J.M. White, *Using photons and electrons to drive surface chemical reactions*. *Journal of Molecular Catalysis A: Chemical*, 1998. **131**(1-3): p. 71-90.
125. S.-W. Hla and K.-H. Rieder, *STM CONTROL OF CHEMICAL REACTIONS: Single-Molecule Synthesis*. *Annual Review of Physical Chemistry*, 2003. **54**(1): p. 307-330.
126. M.A. Walsh and M.C. Hersam, *Atomic-Scale Templates Patterned by Ultrahigh Vacuum Scanning Tunneling Microscopy on Silicon*. *Annual Review of Physical Chemistry*, 2009. **60**(1): p. 193-216.
127. N. Silvis-Cividjian and C.W. Hagen, *Electron-Beam-Induced Nanometer-Scale Deposition*. *Advances in Imaging and Electron Physics*. Vol. 143. 2006: Elsevier. 235.
128. T. Bret, *Physico-chemical study of the focused electron beam induced deposition process*. 2005, EPFL: Lausanne.
129. T. Bret, I. Utke, P. Hoffmann, M. Abourida, and P. Doppelt, *Electron range effects in focused electron beam induced deposition of 3D nanostructures*. *Microelectronic Engineering*, 2006. **83**(4-9): p. 1482-1486.
130. K. Molhave, D.N. Madsen, S. Dohn, and P. Boggild, *Constructing, connecting and soldering nanostructures by environmental electron beam deposition*. *Nanotechnology*, 2004. **15**(8): p. 1047-1053.
131. V.V. Aristov, N.A. Kislov, and I.I. Khodos, *Direct electron-beam-induced formation of nanometer-scale carbon structures in STEM. I. Nature of "long-range" growth outside the substrate*. *Microscopy, Microanalysis, Microstructures*, 1992. **3**(4): p. 313-322.
132. H. Hiroshima and M. Komuro, *Fabrication of conductive wires by electron-beam-induced deposition*. *Nanotechnology*, 1998(9): p. 108.
133. W.F. van Dorp, S. Lazar, C.W. Hagen, and P. Kruit, *Solutions to a proximity effect in high resolution electron beam induced deposition*. *Journal of Vacuum Science & Technology B*, 2007. **25**(5): p. 1603-1608.
134. G. Boero, I. Utke, T. Bret, N. Quack, M. Todorova, S. Mouaziz, P. Kejik, J. Brugger, R.S. Popovic, and P. Hoffmann, *Submicrometer Hall devices fabricated by focused electron-beam-induced deposition*. *Applied Physics Letters*, 2005. **86**(4).

135. N. Silvis-Cividjian, C.W. Hagen, L.H.A. Leunissen, and P. Kruit, *The role of secondary electrons in electron-beam-induced-deposition spatial resolution*. *Microelectronic Engineering*, 2002. **61-62**: p. 693-699.
136. N. Silvis-Cividjian, C.W. Hagen, and P. Kruit, *Spatial resolution limits in electron-beam-induced deposition*. *Journal of Applied Physics*, 2005. **98**(8).
137. M. Takeguchi, M. Shimojo, K. Mitsuishi, M. Tanaka, R. Che, and K. Furuya, *Fabrication of nanostructures with different iron concentration by electron beam induced deposition with a mixture gas of iron carbonyl and ferrocene, and their magnetic properties*. *Journal of Material Science*, 2006. **41**(14): p. 4532-4536.
138. M. Takeguchi, M. Shimojo, and K. Furuya, *Fabrication of Alpha-Iron and Iron Carbide Nanostructures by Electron-Beam Induced Chemical Vapor Deposition and Postdeposition Heat Treatment*. *Japanese Journal of Applied Physics Part 1-Regular Papers Brief Communications & Review Papers*, 2005. **44**(7B): p. 5631-5634.
139. M. Shimojo, M. Takeguchi, and K. Furuya, *Formation of crystalline iron oxide nanostructures by electron beam-induced deposition at room temperature*. *Nanotechnology*, 2006. **17**(15): p. 3637-3640.
140. M. Shimojo, M. Takeguchi, M. Tanaka, K. Mitsuishi, and K. Furuya, *Electron beam-induced deposition using iron carbonyl and the effects of heat treatment on nanostructure*. *Applied Physics a-Materials Science & Processing*, 2004. **79**(8): p. 1869-1872.
141. P.C. Hoyle, J.R.A. Cleaver, and H. Ahmed, *Electron beam induced deposition from W(CO)₆ at 2 to 20 keV and its applications*. *Journal of Vacuum Science & Technology B*, 1996. **14**(2): p. 662-673.
142. P.C. Hoyle, M. Ogasawara, J.R.A. Cleaver, and H. Ahmed, *Electrical resistance of electron beam induced deposits from tungsten hexacarbonyl*. *Applied Physics Letters*, 1993. **62**(23): p. 3043-3045.
143. M. Shimojo, K. Mitsuishi, A. Tameike, and K. Furuya, *Electron induced nanodeposition of tungsten using field emission scanning and transmission electron microscopes*. *Journal of Vacuum Science & Technology B: Microelectronics and Nanometer Structures*, 2004. **22**(2): p. 742-746.
144. R.R. Kunz and T.M. Mayer, *Electron beam induced surface nucleation and low-temperature decomposition of metal carbonyls*. *Journal of Vacuum Science & Technology B: Microelectronics and Nanometer Structures*, 1988. **6**(5): p. 1557-1564.
145. H.W.P. Koops, J. Kretz, M. Rudolph, and M. Weber, *Constructive three-dimensional lithography with electron-beam induced deposition for quantum effect devices*. *Journal of Vacuum Science & Technology B: Microelectronics and Nanometer Structures*, 1993. **11**(6): p. 2386-2389.
146. K. Edinger, T. Gotszalk, and I.W. Rangelow. *Novel high resolution scanning thermal probe*. in *The 45th international conference on electron, ion, and photon beam technology and nanofabrication*. 2001: AVS.
147. G.C. Gazzadi and S. Frabboni, *Fabrication of 5 nm gap pillar electrodes by electron-beam Pt deposition*. *Journal of Vacuum Science & Technology B: Microelectronics and Nanometer Structures*, 2005. **23**(2): p. L1-L3.
148. I. Utke, P. Hoffmann, B. Dwir, K. Leifer, E. Kapon, and P. Doppelt, *Focused electron beam induced deposition of gold*. *Journal of Vacuum Science & Technology B: Microelectronics and Nanometer Structures*, 2000. **18**(6): p. 3168-3171.
149. O. Guise, J. Ahner, J. Yates, and J. Levy, *Formation and thermal stability of sub-10-nm carbon templates on Si(100)*. *Applied Physics Letters*, 2004. **85**(12): p. 2352-2354.
150. A.E. Ennos, *The origin of specimen contamination in the electron microscope*. *British Journal of Applied Physics*, 1953. **4**: p. 101-106.

151. A.E. Ennos, *The sources of electron-induced contamination in kinetic vacuum systems*. British Journal of Applied Physics, 1954. **5**(1): p. 27-31.
152. L. Reimer, *Scanning Electron Microscopy*. 2nd ed. Springer Series in Optical Sciences, ed. H.K.V. Lotsch. Vol. 45. 1998, Heidelberg: Springer-Verlag.
153. L. Reimer and C. Tollkamp, *Measuring the backscattering coefficient and secondary electron yield inside a scanning electron microscope*. Scanning, 1980. **3**(1): p. 35-39.
154. D. Drouin, A.R. Couture, D. Joly, X. Tastet, V. Aimez, and R. Gauvin, *CASINO V2.42-a fast and easy-to-use modeling tool for scanning electron microscopy and microanalysis users*. Scanning, 2007. **29**(3): p. 92-101.
155. I.N. Stranski and L. von Krastanov. in *Acad. Wiss. Lit. Mainz Math.-Natur Kl. 11b 146 797*. 1939.
156. T. Berger, M. Sterrer, O. Diwald, and E. Knozinger, *Charge trapping and photoadsorption of O₂ on dehydroxylated TiO₂ nanocrystals - An electron paramagnetic resonance study*. Chemphyschem, 2005. **6**(10): p. 2104-2112.
157. M.J. Elser, T. Berger, D. Brandhuber, J. Bernardi, O. Diwald, and E. Knozinger, *Particles coming together: Electron centers in adjoined TiO₂ nanocrystals*. Journal of Physical Chemistry B, 2006. **110**(15): p. 7605-7608.
158. A. Botman, J.J.L. Mulders, and C.W. Hagen, *Creating pure nanostructures from electron-beam-induced deposition using purification techniques: a technology perspective*. Nanotechnology, 2009. **20**(37).
159. A. Botman, J.J.L. Mulders, R. Weemaes, and S. Mentink, *Purification of platinum and gold structures after electron-beam-induced deposition*. Nanotechnology, 2006(15): p. 3779.
160. S. Wang, Y.-M. Sun, Q. Wang, and J.M. White, *Electron-beam induced initial growth of platinum films using Pt(PF₃)₃/PF₅*. Journal of Vacuum Science & Technology B: Microelectronics and Nanometer Structures, 2004. **22**(4): p. 1803-1806.
161. K.M. Poole, *Electrode Contamination in Electron Optical Systems*. Proc. Phys. Soc. B, 1953. **66**: p. 542-547.
162. G. Comelli, V.R. Dhanak, M. Kiskinova, N. Pangher, G. Paolucci, K.C. Prince, and R. Rosei, *Adsorption of oxygen on Rh(110) and reactivity of different over-layer structures*. Surface Science, 1992. **269/270**(1-3): p. 360-364.
163. G. Comelli, V.R. Dhanak, M. Kiskinova, N. Pangher, G. Paolucci, K.C. Prince, and R. Rosei, *Adsorption of oxygen on Rh(110): a LEED, Auger electron spectroscopy and thermal desorption study*. Surface Science, 1992. **260**: p. 7-13.
164. G. Comelli, V.R. Dhanak, M. Kiskinova, K.C. Prince, and R. Rosei, *Oxygen and nitrogen interaction with rhodium single crystal surfaces*. Surface Science Reports, 1998. **32**(5): p. 165-231.
165. H. Marbach, S. Gunther, B. Luerssen, L. Gregoratti, M. Kiskinova, and R. Imbihl, *Selforganization of alkali metal on a catalytic metal surface*. Catalysis Letters, 2002. **83**(3-4): p. 161-164.
166. H. Marbach, S. Gunther, T. Neubrand, and R. Imbihl, *Mass transport of alkali metal with pulses: catalytic NO reduction with hydrogen on Rh(110)/K*. Chemical Physics Letters, 2004. **395**(1-3): p. 64-69.
167. H. Marbach, G. Lilienkamp, H. Wei, S. Gunther, Y. Suchorski, and R. Imbihl, *Ordered phases in alkali redistribution during a catalytic surface reaction*. Physical Chemistry Chemical Physics, 2003. **5**(12): p. 2730-2735.
168. A. Lugstein, Y.J. Hyun, M. Steinmair, B. Dielacher, G. Hauer, and E. Bertagnolli, *Some aspects of substrate pretreatment for epitaxial Si nanowire growth*. Nanotechnology, 2008. **19**(48).

169. Y.J. Hyun, A. Lugstein, M. Steinmair, E. Bertagnolli, and P. Pongratz, *Orientation specific synthesis of kinked silicon nanowires grown by the vapour-liquid-solid mechanism*. Nanotechnology, 2009. **20**(12).
170. A. Lugstein, M. Steinmair, Y.J. Hyun, G. Hauer, P. Pongratz, and E. Bertagnolli, *Pressure-induced orientation control of the growth of epitaxial silicon nanowires*. Nano Letters, 2008. **8**(8): p. 2310-2314.
171. Y. Huang, X.F. Duan, Q.Q. Wei, and C.M. Lieber, *Directed assembly of one-dimensional nanostructures into functional networks*. Science, 2001. **291**(5504): p. 630-633.
172. Y. Cui and C.M. Lieber, *Functional nanoscale electronic devices assembled using silicon nanowire building blocks*. Science, 2001. **291**(5505): p. 851-853.
173. F. Porrati, R. Sachser, and M. Huth, *The transient electrical conductivity of W-based electron-beam-induced deposits during growth, irradiation and exposure to air*. Nanotechnology, 2009. **20**(19).
174. M. Huth, D. Klingenberger, C. Grimm, F. Porrati, and R. Sachser, *Conductance regimes of W-based granular metals prepared by electron beam induced deposition*. New Journal of Physics, 2009. **11**.

6 Acknowledgements

A plant needs a fertile soil, water and the sun to grow. Similarly a scientist can not develop confined to himself, input and support from various sources is needed.

First of all I would like to express my sincere gratitude to Prof. Dr. Hans-Peter Steinrück for his mentorship and support. I am not only grateful for the ideal working conditions in terms of scientific environment but also for the pleasant atmosphere at the Lehrstuhl PC II.

I would like to thank Prof. Dr. Patrik Schmuki and Prof. Dr. Andreas Hirsch my other mentors from Erlangen, which accompanied my Habilitation with a genuine positive attitude.

I feel very much connected to my present and former students to whom I am indebted for their committed work in the lab. To see and discuss fresh and in particular unexpected data is probably the most exciting part of our work and finally the fuel that keeps us running. To stick to the order of the thesis I first would like to thank the current members of the STM team: Dr. Florian Buchner, Stefanie Gläbel, Michael Röckert; the former members: Dr. Karmen Commanici, Veronika Schwald, Elisabeth Zillner, Ina Kellner and Christina Drathen; the FEBIP team: Thomas Lukasczyk, Michael Schirmer, Marie-Madeleine Walz, Florian Vollnhals and Achim Sandmann.

In addition I would like to thank the students involved in the AFM polymer blend project, namely Jana Korzekwa, Johannes Hirschmann, Sabine Frühbeisser and all other students involved in one or the other project in the framework of “Mitabeiterpraktika”.

As a young scientist it was and still is a very important and exciting experience to be part of the SFB 583 located in Erlangen, which triggered numerous collaborations. Foremost I would like to acknowledge the very fruitful and important cooperation with Dr. Michael Gottfried and his group members, namely Dr. Ken Flechtner, Yun Bai and Martin Schmid.

The cooperation with the theory group of Prof. Dr. Andreas Görling and Dr. Wolfgang Hieringer as well as with Prof. Dr. Tim Clark and Dr. Tatjana Shubina are greatly acknowledged and yielded important complementary information, which pushed the porphyrin project one step further.

I also thank Dr. Norbert Jux, Prof. Dr. Paul Müller and Prof. Dr. Nicolai Burtzlaff for diverse collaborations and/or valuable input.

Many thanks to the other cooperation partners located in Erlangen not directly related to the SFB 583: Prof. Dr. Ulrich Zenneck, Ilona Jipa, Prof. Dr. Nadeja Popovska and Dr. Christian Papp.

Special thanks to Prof. Dr. Oliver Diwald and his group members for the cooperation with the TiO_x nanostructures and his friendship. I am more than happy that our ways crossed again in Erlangen.

I am also grateful to the external collaborators Dr. Alois Lugstein (TU Wien), Prof. Dr. Michael Huth (Uni Frankfurt), Prof. Dr. Johannes Barth, Dr. Willi Auwärter (both TU München) and Prof. Dr. Manos Mavrikakis (University Wisconsin-Madison).

For fruitful discussions and valuable input I want to thank in particular Prof. Dr. Armin Götzhäuser, Dr. Andrej Turchanin (both Uni Bielefeld), Prof. Dr. Petra Swiderek (Uni Bremen), Prof. Dr. Michael Hietschold (Uni Chemnitz), Prof. Dr. Kees Hagen, Dr. Wilhelm van Dorp (both TU Delft), Dr. Ivo Utke (EMPA, Thun), Dr. Harry Hoster (Uni Ulm) and Prof. Dr. Jörg Libuda (Uni Erlangen).

Certainly my former advisors and mentors were important for my scientific development. I would like to thank Prof. Dr. John T. Yates, Jr. and Prof. Dr. Jeremy Levy for various valuable experiences during my postdoc time in Pittsburgh and for bringing the EBID process to my attention.

My first steps in surface science in Hannover were very exciting and inspiring. I thank Dr. Sebastian Günther (LMU München) and my “Doktorvater” Prof. Dr. Ronald Imbihl (Uni Hannover) very much for that joyful time and ongoing discussions.

Dr. Florian Maier, Dr. Andreas Bayer and our secretaries Sabine Patzak and Brigitte Heupel took the vast majority of the administrative load from my shoulders, which I very much appreciate and acknowledge.

Very special thanks to our excellent electronic technician Hans-Peter Bäumler for the repair of various hopeless cases and his incredible “magic touch”, he is also dear to my heart as a neighbor and keeper of the fridge.

I am thankful for the many accurate constructions and manifold support of the mechanical workshop headed by Friedhold Wölfel.

It is a great pleasure to work with Bernd Kress. I particularly would like to acknowledge his contribution to the construction and assembly of “Jutta”, our new FEBIP gas handling chamber.

I shall not forget to thank my officemate Dr. Karifala Dumbuya especially for the numerous joyful and interesting conversations beyond science and in the same respect I thank all members of the Lehrstuhl PC II for the friendly atmosphere.

Financial support is greatly acknowledged by the DFG through the SFB 583 and the individual grant MA 4246/1-1.

Last but not least I would like to sincerely thank my parents for supporting me especially during my student years in Dortmund.

Many thanks and a big hug to my lovely wife Zeynep for her support.